Accelerating the Discovery of Novel Metal Organic Chalcogenolates: A Computational and Machine Learning-Driven Approach

by

Adriana J. Ladera

B.S. in Computer Science, University of South Florida (2022)

Submitted to the Center for Computational Science and Engineering
in partial fulfillment of the requirements for the degree of

MASTER OF SCIENCE IN COMPUTATIONAL SCIENCE AND ENGINEERING

at the

MASSACHUSETTS INSTITUTE OF TECHNOLOGY

February 2025

© 2025 Adriana J. Ladera. This work is licensed under a CC BY-NC-ND 4.0 license.

The author hereby grants to MIT a nonexclusive, worldwide, irrevocable, royalty-free license to exercise any and all rights under copyright, including to reproduce, preserve, distribute and publicly display copies of the thesis, or release the thesis under an open-access license.

Authored by:	Adriana J. Ladera Center for Computational Science and Engineering January 17, 2025
Certified by:	Tess Smidt Asst. Prof. of Electrical Engineering & Computer Science, Thesis Supervisor
Accepted by:	Nicolas Hadjiconstantinou Professor of Mechanical Engineering Co-Director, Center for Computational Science and Engineering

Accelerating the Discovery of Novel Metal Organic Chalcogenolates: A Computational and Machine Learning-Driven Approach

by

Adriana J. Ladera

Submitted to the Center for Computational Science and Engineering
on January 17, 2025 in partial fulfillment of the requirements for the degree of

MASTER OF SCIENCE IN COMPUTATIONAL SCIENCE AND ENGINEERING

ABSTRACT

Metal Organic Chalcogenolates (MOChas) are a class of robust, self-assembling, and hybrid materials featuring inorganic metalo-chalcogen frameworks that are scaffolded by organic ligands. These low-dimensional structures exhibit tunable optoelectronic properties, making them promising candidates for various applications, including optical sensors and nanotechnology. This tunable relationship between MOCha structural arrangements and targeted properties opens up a vast yet challenging search space for novel MOCha structures. Density Functional Theory (DFT) can predict properties of materials with good accuracy, making it a powerful choice for even hypothetical materials. However, the discovery of novel MOChas structures is constrained by poor scalability of DFT relaxation times for large systems and a lack of high-throughput design methods that can capture the complex geometries of MOChas. In this work, we employ DFT calculations to investigate the energetic and electronic properties of various MOChas, and provide insight into the optical behavior and kinetic favorability of such structures. To address the computational bottlenecks of high-throughput design and DFT workloads, we discuss the use of machine-learned interatomic potentials and various generative models that can enable rapid prototyping of novel MOCha structures.

Thesis supervisor: Tess Smidt
Title: Asst. Prof. of Electrical Engineering & Computer Science

Acknowledgments

This thesis is a conglomeration of the insightful and chaotic journey that was my master's degree. I'm incredibly grateful to see my growth and progress as a scientist, and look forward to the future of contributing to the fields of computational and materials science. Even now, I still cannot express how grateful I am to be able to work alongside many brilliant minds at MIT, but I certainly couldn't have done it without my amazing support group.

I would like to thank my academic family first and foremost for helping me navigate this path through the world of science. To my current research advisor Prof. Tess Smidt and my undergraduate research advisors, Prof. Inna Ponomareva and Prof. Heather Kulik, thank you for your guidance, and for being the powerful women role models in STEM that I look up to. Thank you as well to Prof. Long-Qing Chen, Dr. Bo Wang, Dr. Chenru Duan, and Dr. Vyshnavi Vennelakanti, for working closely with me and for being such great mentors while I was still very new to this whole science thing. To the lively environment that is the Atomic Architects lab, thank you all for climbing, lifting, and going to EDM concerts with me, and for making me even more nerdy. A special thank you as well to Prof. Nate Hohman and his lab, for your exciting and welcoming energy, and for allowing me to distort your beautiful materials.

To my friends outside of the lab, thank you for making life in Boston much more adventurous. I truly enjoy hiking, cooking, crafting, and camping with you all. And to my dear beloved friends whom I share precious time with in Florida— Spaino, the Test Tickles, Chantal, Bucci, the Pookies, and Remy's Angels,– thank you for growing with me for several years and for making Florida such an exciting place to visit. To Miss Mary– thank you for helping me find tools to work around my ADHD, and to not see it as a hindrance (inattentive, chatty, distracting) but as a unique feature of myself (hobby-searching, sociable, and high-energy)! Finally, thank you to my family and loved ones– my cuzzos, mom, dad, Giz, Bing, Bobbie, and of course my dear feline void Portobello– thank you for being my source of guidance, healing, comfort, and for helping to shape me into who I am today.

This research is based upon work supported by the National Science Foundation Graduate Research Fellowship Program (NSF GRFP) under Grant No. 2141064. This research also uses resources from the National Energy Research Scientific Computing Center (NERSC), a Department of Energy Office of Science User Facility using NERSC award ASCR-ERCAP-0033907, and the Department of Energy Integrated Computational and Data Infrastructure (DOE ICDI) under Grant No. DE-SC0022215.

Contents

Title page **1**

Abstract **3**

1 Introduction **11**

2 Methods **15**
- 2.1 Density Functional Theory 15
- 2.2 Calculation Details 18
- 2.3 Modification of Structures 20

3 Don't Sugar Coat it..or do... **23**
- 3.1 Introduction 23
- 3.2 Methods 24
- 3.3 Results and Discussion 25
- 3.4 Conclusion 35

4 Functional Group Drivers and Silver MOCha Passenger Princesses **37**
- 4.1 Introduction 37
- 4.2 Methods 38
- 4.3 Results and Discussion 39
- 4.4 Conclusions 50

5 AI'll be back– machine-learning accelerated materials design **51**
- 5.1 Structure Generation for Novel Materials 52
- 5.2 Fine-tuned ML-interatomic potentials 53
- 5.3 Closing Remarks 54

A Relevant Terms **55**
- A.1 Relevant Terms 55

B Appendix for Don't Sugar Coat it..or do... **57**
- B.1 Figures 57

C Appendix for Functional Group Drivers and Silver MOCha Passenger Princesses **63**

References67

List of Figures

2.1 **(A)** Procedure for constructing the inorganic only, in which atomic species that make the ligand are removed and the ligand is replaced with a hydrogen. **(B)** Procedure for creating a hypothetical MOCha. 21

3.1 Computational dehydration process of sugar MOChas, shown here specifically for the glucose MOCha system. Blue solid-line circles encase water molecules, whereas blue dotted-line circles encase water molecules that will be dehydrated, i.e. “computational dehydration". Red solid-line ovals encase Ag-O bonds that are present in compound **3**, but not in **1**. 25

3.2 **(A)** Material design of chiral bioinorganic MOChas: multiple chiral, hydroxyl, and only one different stereocenter at carbon 4 (highlighted in orange oval) between glucosethio and galactosethio; the bottom panel illustrates sugar MOCha self-assembly via silver ions with sugar ligands. **(B-C)** Scanning electron micrographs (SEM) of both silver (I) thioglucose dihydrate (**1**) and silver (I) thiogalactose dihydrate (**2**), respectively. **(D)** Crystal structure of silver (I) thioglucose dihydrate (**1**). **(F)** Crystal structure of silver (I) thiogalactose dihydrate (**2**). **(E)** silver (I) thioglucose monohydrate (**3**). **(G)** Crystal structure of anhydrous silver (I) thiogalactose (**4**). Color code: Ag, silver; S, yellow; O, red; C, black; Water, purple. Hydrogen atoms have been omitted for clarity. 27

3.3 Optical properties of **1** and **2**. **(A)** Absorption and PL spectra of **1** and **2** at room temperature. The photographs of **1** and **2** under UV light are shown in the inset: **1** is highlighted in a rectangular blue frame, and **2** is highlighted in a rectangular green frame. **(B)** Time-resolved PL decays of **1** and **2** along with the decay. **(C)** circular dichroism (CD) spectra for **1**, **2**, and the control sample 2MMB, respectively. **(D-F)** CPL spectra of **1**, **2**, and the control sample 2MMB were excited at 350 nm, respectively. 29

3.4 **(A-D)** Electronic structure of compounds **1-4**, respectively. For each structure, the left inset shows the band diagram, where orange bands represent inorganic interactions, black bands represent organic interactions, and interpolated colors indicate mixed inorganic-organic interactions. Blue and green points highlight the wave vectors at which the CBM and VBM occur, respectively. The middle panel presents the density of states (DOS), separated by atomic species. The middle inset displays the Brillouin zone *k*-path for the visualized band structure. The right panel displays partial charge densities at the CBM for each compound, with some other parts of the unit cell and water molecules omitted for clarity. Note that figures with a larger number of bands correspond to MOChas with a larger number of atoms. 32

3.5 Kinetic uptake/release of water in glucose MOCha system. **(A)** TGA curves of glucose MOCha **1** and **3**, with a zoom in the inset. **(B)** Emission spectra show the chromogenic transition of initial **1** from blue to green **(3)** during dehydration in ethanol solvent (1 mg/2 mL). **(C)** Emission spectra show the chromogenic transition of initial **3** from green to blue (1) during rehydration in water solvent (1 mg/2 mL). **(D)** Comparison between **1** (left panel, highlighted in green) and **3** (right panel, highlighted in purple), focusing on the asymmetry unit (upper panel) and AgS network (lower panel). 35

4.1 Graphical abstract showcasing the structural, luminescent, and electronic trends across silver benzenethiolate MOCha series. 37

4.2 **(A-D)** Example morphologies of compounds **1-4**, with the ligand inset. **(E)** Normalized emission spectra of the four MOChas. Compound **4** is the only photoluminescent MOCha with a maximum emission peak at 589 nm. **(F)** Solid-state powder samples of compounds **1**–**4** illuminated with ultraviolet light. **(G-J)** Resolved structures for compounds **1-4**. . . 39

4.3 Structural arrangement of the various AgSPh-X inorganic AgS topologies. **(A)** 2D sheet of AgSPh-*p*-OCH_3, with edge-sharing tetrahedral surfaces. **(B)** Slight buckling in the 2D sheet of AgSPh-*m*-OH, characterized by the large open rings in the structure highlighted in light blue. Red triangles over the polyhedral illustration demonstrate the pattern of trigonal, near-planar geometry. Grey dashed and dotted ghost bonds show the typical 2D inorganic connectivity. **(C)** Large buckling of the 2D inorganic structure in AgSPh-*m*-NH_2. Highlighted red triangles and blue lines in the polyhedral illustration show the presence of trigonal pyramidal and bent geometries, respectively. **(D)** 1D rods of AgSPh-*m*-OCH_3, signaled by tubes of connected trigonal planes. 42

4.4 DFT self-consistent field calculations on relaxed geometries, highlighting the energy difference per formula unit between the transitional AgSPh-*m*-NH_2 and its 2D and 1D homologues of the same ligand **(A)**. The same is done for AgSPh-*m*-OH **(B)**. **(C)** Hypothetical MOCha models of the 1D AgS structure paired with 3-aminothiophenol (left) and 3-(dimethylamino)thiophenol (right), the latter of which has a crystallographically-unresolved structure. 43

4.5 **(A-D)** Electronic structure calculations for the AgSPh-X series. Left inset is the band diagram, in which orange bands indicate inorganic interaction and black bands indicate organic interaction, with interpolated colors representing mixed interaction. Blue and green points indicate the wave vector where the conduction band minimum and valence band maximum occur, respectively. Right inset is the normalized density of states, separated by atomic species. Note that figures with a larger number of bands correspond to MOChas with a larger number of atoms. 45

4.6 Partial charge densities at the valence band maximum (VBM) and conduction band minimum (CBM). **(A)** AgSPh-*p*-OCH_3. **(B)** AgSPh-*m*-OH. **(C)** AgSPh-*m*-NH_2– note that the other half of the motif for the unit cell is omitted for clarity. **(D)** AgSPh-*m*-OCH_3. 48

B.1 **(A)** The inorganic nanowire of compound **1** consists of repeating Ag_4S_4 units. The Ag_4S_4 units are linked via four Ag-S bonds, forming a 1D chain. **(B)** Each Ag_4S_4 unit features a chiral pyramidal Ag_4 core where each silver atom is coordinated to two or three other silver atoms at different Ag-Ag distances. Color code: Ag, Silver; S, Yellow. 57

B.2 The inorganic AgS core of compound **3** retains a similar 1D Ag-S arrangement as compound **1**, composed of repeating Ag_4S_4 units **(A)** with chiral pyramidal Ag_4 motifs **(B)**. Color code: Ag, Silver; S, Yellow. 58

B.3 **(A)** Compound **1** is viewed along the *c* axis and **(B)** Compound **2** is viewed along the *b* axis. Light blue polygons highlight the inorganic topologies and hydrogen bonding interactions of the molecules, whereas light red circles enclose the galactose and glucose ligands. Color code: Ag, silver; S, yellow; O, red; C, brown; H, pink. **(C)** structure of 1D chain unit and S-Ag-S angle in glucose MOCha **1**. **(D)** structure of 1D chain unit and S-Ag-S angle in galactose MOCha **2**. There are H-bonds (OH···O) among ligands and water molecules in both glucose and galactose MOChas. In **2**, there are interchain and intrachain H-bonds, whereas there are only interchain H-bonds in **1**. The O-H···O hydrogen bonds in **2** have a distance of 1.982 Å, indicating directional hydrogen bonds of hydroxyl groups in the sugar ligands. This leads to an increase in the angle of the sulfur-silver-sulfur bond compared to glucose MOCha **1** which lacks interchain hydrogen bonds of the hydroxyl group. As a result, the sulfur-sulfur distance is longer in MOCha **2** (dS-S = 4.698 Å) than in **1** (dS-S = 4.389 Å), decreasing the coordination number of silver-sulfur (CN = 2 in galactose; CN = 3 or 4 in glucose MOCha **1**) and reducing the symmetry of the crystal system compared to the glucose MOCha. In this case, we observed that the secondary structure, driven by the hydrogen bonding network, affects the primary structure of the Ag-S network in a manner similar to biological geometry. 58

B.4 The Ag-O interaction distances are shown in compounds **1** **(A)** and **2** **(B)**. High luminescence in silver(I) methyl 2-mercaptobenzoate compounds, has been linked to Ag-O interactions, which we recently reported as correlating with relatively high quantum yields. In compounds **1** and **2**, a similar close association is observed between silver and the bridging oxygen atoms of the sugar ligands, with Ag-O bond lengths ranging from 2.741 to 2.827 Å. These distances are notably shorter than the sum of the van der Waals radii (3.24 Å), suggesting the presence of a strong interaction that may contribute to the observed luminescence properties. 59

B.5 **(A-D)** VBM partial charge densities for each compound **1-4**, respectively, with some other parts of the unit cell and water molecules omitted for clarity. 60

B.6 Comparison of PXRD patterns between as-synthesized hydrated silver thioglucose dihydrate **1**, partially dehydrated silver thioglucose monohydrate **3**, and rehydrated silver thioglucose dihydrate **1**, demonstrating that dehydration and rehydration are reversible. 61

B.7 **(A)** TGA curves of compounds **2** and **4**. **(B)** Comparison of PXRD patterns between as-synthesized hydrated silver thiogalactose dihydrate **2**, fully dehydrated silver thiogalactose **4**, and the rehydrated galactose MOCha. **(C)** Emission spectra comparing the **2** and **4**. The as-synthesized **2** was heated in a vacuum oven at 90 °C for 24 hours to release water, resulting in fully dehydrated samples **4** (Fig. A). PXRD patterns revealed that the **4** exhibits few distinct phases and does not revert to the hydrated state **2** after rehydration, suggesting an irreversible solid-solid phase transformation from galactose MOCha hydrates to dehydrated forms. Fig. **C** shows no significant change in emission between dihydrate **2** and anhydrous **4** under 350 nm excitation. 61

B.8 **(A)** UV-vis spectra comparing compounds **2** and **4**. **(B)** Comparison between **2** (left panel, highlighted in orange) and **4** (right panel, highlighted in blue), focusing on the asymmetry unit (upper panel) and Ag-S network (lower panel). In compound **4**, the Ag-Ag interactions strengthen, forming a coordination number (CN(Ag-Ag)) of 5. This represents a significantly different silver core environment compared to the hydrated form **2** (Fig. **B**), suggesting a change in the electronic structure, indicated by the UV-vis spectrum. Importantly, the change in the Ag-Ag system occurs without altering the inorganic Ag-S arrangement, which remains as double helices. Notably, the asymmetry unit of dehydrated galactose MOCha does not contain water, in line with TGA experiments in Fig. A. . . . 62

C.1 Brillouin zones for the selected k-paths. 63
C.2 **(A-D)** Band structure diagrams for the inorganic structure, indicated in orange. All structures effectively have a direct band gap at the Γ point. 64
C.3 Partial charge densities at the VBM and CBM for AgSPh-m-OH, viewed along the a-axis. Electron delocalization of the participating Ag(d) orbitals is encircled in light blue. . . . 65

Chapter 1

Introduction

Metal chalcogenolate-based materials play a significant role across diverse scientific fields, including molecular chemistry, coordination chemistry, and nanotechnology. Understanding these materials at the intersection of these fields is therefore crucial for designing and optimizing their targeted properties [1]. These compounds have the general formula $[\mathrm{M}_x(\mathrm{ER})_y]_\infty$, where "M" is a late- or post-transition metal–most commonly a d^{10} coinage metal (Cu, Au, Ag), "E" denotes a chalcogen (S, Se, Te), and "R" signifies any organic side group. MOChas are often low-dimensional, featuring 0D oligomers and 1D and 2D coordination polymers, in which the dimensionality is based on the inorganic structural topology [2]. Previously, structure-composition-function relationships have been explored for a variety of these compound systems [3, 4]. The inorganic structure and the packing of the organic components in these materials are determined by the selection of the organic ligands, and each organic ligand constitutes a unique semiconductor with properties related to the topology of the inorganic phase. Because of the strongly excitonic nature of the material system, crystal engineering by ligand editing is an attractive approach for modifying the optoelectronic properties of the material system. Furthermore, the d^{10} coinage metals are equally important in property tuning and are used in materials that self-assemble and emit light, leading to applications in devices such as optical sensors [5].

Under this class of materials are Metal Organic Chalcogenolates (MOChas), which are hybrid structures composed of an inorganic metal-chalcogen framework, arranged in a polyhedral manner, and scaffolded by organic ligands. The inorganic and organic components are bonded through covalent interactions, and van der Waals forces facilitate the assembly of these hybrid motifs into the crystal structure. The choice of ligand drives the distortion of the inorganic topology as well as their optoelectronic properties, making MOChas a compelling class of materials for investigating structure-property relationships and tunability of targeted properties [3, 4]. Additionally, the functionality and packing of the ligand within the MOCha crystal, unique interactions between the metal and organic chalcogenolate, and the presence of metallophilic interactions and hydrogen bonds result in a rich variety of MOCha structures [4]. By manipulating the coordination modes, ligand choice, and selection of coinage metals, we can tune the resulting luminescent, electronic, and structural characteristics for a wide variety of MOChas.

Density Functional Theory (DFT) can be used to explore the electronic and energetic properties of both synthesized and hypothetical MOChas, as well as relax the structures to equilibrium. As DFT is *ab initio*, it can predict electronic properties of atomic arrangements at the ground state with good accuracy, making it a great choice for investigating hypothetical structures.

In this work, we utilize DFT calculations in collaboration with experiments to understand the connections between electronic and energetic properties and structural features in biochiral MOChas with fluorescent asymmetry. We focus on thiocarbohydrates, and precipitate silver ions with sugar ligands to form silver(I) thioglucose dihydrate and silver(I) thiogalactose dihydrate. Dehydration is reversible and yields silver(I) thioglucose monohydrate and anhydrous silver(I) thiogalactose. Previously, 1D MOChas have been reported with yellow to orange fluorescence, but here each compound forms a 1D MOCha structure with intense blue or green luminescence. Importantly, the difference of the hydroxyl position in the glucose and galactose derivatives resulted in entirely different luminescent and hydration properties for the two structures. We show that the inorganic centers are themselves chiral in both compounds. DFT modeling revealed that the dehydration in the galactose MOCha system is energetically more favorable than the glucose MOCha system, predicting reversible dehydration in glucose-based MOChas and irreversible dehydration in galactose-based MOChas. The optical shift is attributed to atomic displacements in silver thioglucose during water release/uptake, altering the electronic structure and energetics. These findings highlight structure-property relationships that may extend to other bioinorganic systems and offer promise for applications such as 3D displays, spintronics, and cancer diagnostics [6, 7, 8], due to their chirality, biocompatibility, and biofunctionalization potential [9, 10].

Also in collaboration with experiments, we investigate the electronic, structural, and luminescent properties of silver benzenethiolate (AgSPh-X) MOChas, where X represents the functional group and its position on the phenyl ring. The study highlights the critical role of ligand functional groups in determining the topology of MOChas, ranging from 2D to 1D structures. Four MOChas are examined: 2D silver *para*-methoxybenzenethiolate (AgSPh-p-OCH_3), 1D silver *meta*-methoxybenzenethiolate (AgSPh-m-OCH_3), and two intermediate topologies– silver *meta*-hydroxythiophenolate (AgSPh-m-OH) and silver *meta*-aminothiophenolate (AgSPh-m-NH_2)– that capture the range between 2D and 1D structures. We find that the functional groups influence the structural formation of silver benzenethiolate MOChas but do not directly participate in the resulting electronic properties and luminescent properties. Hypothetical 2D and 1D MOCha models containing m-OH and m-NH_2 functional groups were created and analyzed using DFT calculations, revealing that the experimental AgSPh-m-NH_2 and AgSPh-m-OH are energetic and structural intermediates between the 2D and 1D prototypes. In other words, DFT energetics calculations predict that the 1D topology for these functional groups is the most energetically favorable, but additional factors may drive the kinetic formation of the actual synthesized structures. We hypothesize that methyl groups will disrupt the amine hydrogens from kinetically stabilizing AgSPh-m-NH_2 and collapse the inorganic structure into a 1D topology. Indeed, the crystallite morphology of this newly synthesized silver *meta*-(dimethylamino)thiophenolate appears to be 1D, validating our hypothesis and showcasing the predictive power of DFT. Additionally, trends in electronic band gaps, conduction band electron delocalization, and luminescence support the progression from 2D to 1D inorganic dimensionality across the AgSPh-X series.

Due to the tunable relationship between MOCha structural arrangements and targeted properties, the search space for novel structures remains large. Design avenues for novel

MOCha structures include selection and manipulation of the inorganic topology and the ligands. From the inorganic avenue, the species of synthesized MOChas can be substituted, the distortion of inorganic topologies can be parameterized, and several periodic inorganic structures with varying arrangements can be generated. Additional consideration must be placed on the ligand as well–the choice of ligand induces inorganic structural distortion, but so do selections as simple as the functional group and positions on the ligand.

Nevertheless, exploring new combinations of inorganic topologies and organic ligands is challenging. The task demands the construction of novel and chemically-valid geometries that incorporate the complexities of MOCha properties (hydrogen bonding, van der Waals forces, metallophilic interactions). Current attempts to construct hypothetical MOChas involve substitution of inorganic species and ligands with the aid of a coordinate skeleton and DFT relaxation of these hypothetical structures. Even DFT relaxations prove to be a computational bottleneck, as accurate DFT modeling is computationally-intensive. To address these design questions, we conclude with a discussion on the possibilities of generative models for producing novel inorganic structures and ligand packing patterns, and machine-learned interatomic potentials (MLIPs) that can reduce the number of DFT calculations required for MOCha relaxations.

We hope to extend this current research to create an accelerated design workflow for MOChas that can generate, relax, and screen chemically and periodically valid novel MOChas. With this workflow, we can enable fast feedback loops between ML rapid prototyping, experimental synthesis, and DFT-based characterization for a vast range of functional materials.

Chapter 2

Methods

2.1 Density Functional Theory

The work in this thesis primarily relies on density functional theory (DFT) to understand the electronic properties of experimentally-realized MOChas, as well as evaluate and relax the geometries of experimental and hypothetical structures. DFT is based on the Schrödinger wave equation, $\hat{H}\Psi = E\Psi$, where $\hat{H}$ is the Hamiltonian operator that represents the total energies of the system and Ψ is a set of eigenstates (or solutions) for the Hamiltonian. The Schrödinger equation can dictate many properties of a system, such as its most stable geometries, kinetic and potential energies, and electronic energy levels [11]. However, this equation is unfortunately only practical for very simple physical systems, as more realistic and complex difficulties arise due to the many-body quantum effect [12]. This is a consequence of the fact that the wave equation is a partial differential equation containing $3N$ variables, where N is the number of electrons in the system. One can imagine that this kind of computation scales quite sadly for systems as large and as complex as MOChas–whose metal-ligand interactions and large system sizes yield a complex electronic structure composed of hundreds of electrons.

The Born-Oppenheimer approximation greatly simplifies this by representing the atomic nuclei and electrons as separate mathematical problems [11]. This approximation states that the mass of an electron and the mass of an atomic nuclei differ by at least 3 orders of magnitude, such that if given the same kinetic energy, the electron travels at least three orders of magnitude faster relative to that of an atomic nuclei, thereby making the nuclei appear static with respect to the electron. Consider the case of finding the lowest energy configuration, or ground-state, of the electrons moving in the field of a set of atomic nuclei. The problem can then be split into both an electronic and nuclear part. The electronic part can be solved by treating the nuclei as fixed, solving it repeatedly as the nuclei change in small steps. The ground-state energy can then be expressed as a function of the atomic coordinates. We can model the system of multiple electrons interacting with multiple nuclei with the following updated $\hat{H}$ in the Schrödinger equation:

$$\left[\frac{h^2}{2m}\sum_{i=1}^{N}\nabla_i^2 + \sum_{i=1}^{N}V(\vec{\mathbf{r}}_i) + \sum_{i=1}^{N}\sum_{j<i}U(\vec{\mathbf{r}}_i,\ \vec{\mathbf{r}}_j)\right]\Psi = E\Psi \tag{2.1}$$

where m is the electron mass, and the three terms in the brackets describe the kinetic energy of the electrons, the interaction energy between each electron and the collection of atomic nuclei, and the interaction energy between different electrons, respectively. As the above describes the electronic Hamiltonian, the electronic wave function is therefore a function of the spatial coordinates of the N electrons, $\Psi = \Psi(\vec{\mathbf{r}}_1, ..., \vec{\mathbf{r}}_N)$.

Note that the wave function for any particular set of coordinates cannot be directly observed. Rather, what is "measured" is the probability that the N electrons are at a particular set of coordinates $(\mathbf{r}_1, ..., \mathbf{r}_N)$. Important to DFT is the electron density in a given region, $n(\vec{\mathbf{r}})$, which can be expressed as

$$n(\vec{\mathbf{r}}) = 2\sum_i \Psi_i^*(\vec{\mathbf{r}})\Psi_i(\vec{\mathbf{r}}) \tag{2.2}$$

where $\Psi_i^*(\vec{\mathbf{r}})\Psi_i(\vec{\mathbf{r}}) = |\Psi(\vec{\mathbf{r}}_1, ..., \vec{\mathbf{r}}_N)|^2$, the probability that there are N electrons at a given set of atomic coordinates. Compared to the $3N$ variables that exist in a wavefunction, the electron density $n(\vec{\mathbf{r}})$ is a function of only 3 spatial coordinates, which greatly reduces the complexity of the system while still retaining the information that is physically observable from the full wave function solution to the Schrödinger equation.

Kohn and Hohenburg proved two fundamental theorems of DFT, specifically, (i) the ground state energy E of the Schrödinger equation is a unique functional of the electron density $n(\vec{\mathbf{r}})$, and (ii) the electron density that minimizes the energy of the overall functional is the true electron density corresponding to the full solution of the Schrödinger equation [11, 13]. The energy functional can be written in terms of the wave functions, such that

$$E[\{\Psi_i\}] = E_{known}[\{\Psi_i\}] + E_{XC}[\{\Psi_i\}] \tag{2.3}$$

$$E_{known}[\{\Psi_i\}] = \frac{h^2}{m}\sum_i \int \Psi_i^* \nabla^2 \Psi_i d^3r + \int V(\vec{\mathbf{r}})n(\vec{\mathbf{r}})d^3r + \frac{e^2}{2}\iint \frac{n(\vec{\mathbf{r}})n(\vec{\mathbf{r}}')}{|\vec{\mathbf{r}} - \vec{\mathbf{r}}\,'|}d^3r d^3r' + E_{ion} \tag{2.4}$$

The terms of $E_{known}[\{\Psi_i\}]$ correspond to the electron kinetic energies, electron-nuclei Coulomb interactions, electron-electron Coulomb interactions, and ion-ion (or nuclei pair) interactions, respectively. $E_{XC}[\{\Psi_i\}]$, the exchange-correlation functional, is an umbrella term for all the quantum mechanical effects not included in $E_{known}[\{\Psi_i\}]$.

Kohn and Sham [12] demonstrated that obtaining the correct electron density involves the following set of equations that only include a single electron of the form:

$$\left[\frac{h^2}{2m}\nabla^2 + V(\vec{\mathbf{r}}) + V_H(\vec{\mathbf{r}}) + V_{XC}(\vec{\mathbf{r}})\right]\Psi_i(\vec{\mathbf{r}}) = \epsilon_i \Psi_i(\vec{\mathbf{r}}) \tag{2.5}$$

$$V_H(\vec{\mathbf{r}}) = e^2 \frac{n(\vec{\mathbf{r}}')}{|\vec{\mathbf{r}} - \vec{\mathbf{r}}\,'|}d^3r' \tag{2.6}$$

$$V_{XC}(\vec{\mathbf{r}}) = \frac{\partial E_{XC}(\vec{\mathbf{r}})}{\partial n(\vec{\mathbf{r}})} \tag{2.7}$$

Note that the Kohn-Sham equations are very similar to Eq. 2.1. The only exception is that the Kohn-Sham equations are missing summations that appear inside the full Schrödinger equation 2.1, because the solutions of the Kohn–Sham equations are only single-electron wave functions. Here, $V(\vec{\mathbf{r}})$ is the potential describing electron-nuclei interactions. $V_H(\vec{\mathbf{r}})$ is the Hartree potential, which describes the Coulomb repulsion between the electron and the total electron density, and therefore includes a self-interaction contribution between the electron and itself that is not physically meaningful. Therefore, the correction for this term is included in V_{XC}, the potential for the exchange and correlation contributions. The process of Kohn-Sham (KS) DFT is then solved iteratively. First, we begin by choosing an initial electron density, $n_0(\vec{\mathbf{r}})$. Then, $n_0(\vec{\mathbf{r}})$ is used to obtain the wave functions $\Psi_i(\vec{\mathbf{r}})$. Next, we calculate Eq. 2.5 for the Kohn-Sham electron density $n_{KS}(\vec{\mathbf{r}})$ as defined by the single-particle wave functions. Finally, we compare $n_{KS}(\vec{\mathbf{r}})$ to $n_0(\vec{\mathbf{r}})$. If the densities are the same, then $n_{KS}(\vec{\mathbf{r}})$ is the ground-state electron density; otherwise, this calculated $n_{KS}(\vec{\mathbf{r}})$ becomes the new initial electron density and the process repeats iteratively until a ground-state is found.

Density Functionals

While the exact form of E_{XC} is unknown, density functionals have proven to be quite useful for its approximations. Various density functionals have specific ways of treating E_{XC}. An analogous method to visualize the density functionals is to think of them as a "ladder" of approximations, also known as "Jacob's ladder" [14]. In this visual, climbing up the "rungs" of the ladder represents incorporating the details of the lower rungs, or simpler density functionals, but with additional terms. Lowest on the ladder is the group of local density approximations (LDA), the simplest form of density functionals. Here, the exchange correlation energy density depends only on the density at a point and is that of the uniform electron gas of that density.

Unlike the assumptions of LDA, in which systems are viewed as a homogeneous electron gas, in reality most material systems are inhomogeneous with varying spatial density. As such, generalized gradient approximation methods (GGAs) take into account not only the electron density but also the gradient of the density [15, 16]. In this thesis, we use the Perdew-Burke-Ernzerhof (PBE) functional [17], which is a part of a group of GGA methods pushed by Perdew [15, 18, 19, 20, 21, 17] that consider E_{XC} to be derived directly from quantum mechanics principles, including correct limits for various densities, scaling relations, and exact relations on exchange and correlation holes. PBE tends to overestimate lattice parameters [16] and underestimate the band gap [16, 22]. Additionally, PBE is neither the most accurate GGA for bulk solid lattice parameters [23] or for small molecules [24]. However, while its accuracy is limited, we work with the PBE functional because it is less computationally-intensive, the most universal GGA, and works for a wide range of systems. Finally, to correct the absence of long-range van der Waals dispersion interactions in PBE, the DFT-D3 dispersion correction [25] is implemented.

More complex density functionals exist, such as meta-GGAs, hybrid GGAs, and hybrid meta-GGAs, and will be used in the near future to iterate on the work presented in this thesis. However, such functionals are more computationally demanding and therefore not explored for the purposes of this work.

2.2 Calculation Details

All calculations were performed using the Vienna Ab Initio Simulation Package (VASP) [26], the PBE functional [17], and the DFT-D3 dispersion correction [25]. VASP uses a plane-wave basis set; the plane-wave energy cutoff of all calculations is 1.3 × the maximum value of all ENMIN and ENMAX as described in the POTCAR file, in units of eV. Additional terms not defined in this section are reviewed in Appendix A.

Self-Consistent Fields

The purpose of a self-consistent field (SCF) calculation is to solve the Kohn-Sham equations iteratively in order to achieve a consistent and stable electronic charge density given some specified atomic configuration. The SCF cycle ensures that the input and output charge densities are self-consistent within a defined convergence criterion (i.e. electronic loop precision). This convergence ensures that the electronic structure calculations accurately reflect the ground-state electron distribution for the given atomic positions. Specific outputs derived from the SCF calculations, such as charge density (CHGCAR) and WAVECAR files, are often used as inputs for the DOS, band, and charge density calculations, and must be treated accordingly.

For the SCF calculation, an electronic loop precision of 1e-7 eV is used. Since the calculation is static, the crystal structure does not update (the number of ionic steps is zero). The unit cell shape and volume also do not change. Gaussian smearing is turned on with a width of 0.03 eV. For the density of states and band structure calculations, a memory-conserving symmetrization of the charge density is used, whereas symmetrization is turned off completely for the WAVECAR input that will create the partial charge density calculations. This is because the partial charge is calculated from selected k-points and bands, in which symmetrization can lead to misleading results due to incorrect k-point weights.

Structural Relaxation

Structural relaxation is performed in order to optimize the geometry of the MOChas, in which the ground-state energy configuration is obtained. Relaxation consists of two loops, an outer loop that updates the atomic positions and an inner electronic loop consisting of an SCF calculation. To relax MOCha geometries, the conjugate gradient method was used with a stopping criterion of 0.01 eV/Å on all atoms. Gaussian smearing was turned on with a width of 0.03 eV. Finally, the convergence criteria are defined by an electronic loop precision of 1e-6 eV and an ionic loop break condition of -0.01 eV/Å, when the forces on each atom are minimized to this specified tolerance criterion.

Density of States (DOS) and Band Structure

The density of states (DOS) is the number of different states at a particular energy level that electrons are allowed to occupy, whereas the electronic band structure describes the range of energy levels that electrons may have or not have within a crystal. Forbidden energy ranges are called band gaps, which separate the valence band edge (the highest electron-occupied band) and the conduction band edge (the lowest electron-unoccupied band). The minima and maxima of these band edges can dictate whether or not a material has a direct band gap; if the valence band maximum (VBM) and conduction band minimum (CBM) are aligned at the same point in the band structure, then the band gap is direct, and if not, then the band gap is indirect and may require additional analysis from electron-phonon coupling. Conductors, such as metals, do not have band gaps, resulting in high electrical conductivity, whereas insulators have quite large band gaps, and feature poorer conductivity due to electrons having insufficient energy to jump from the valence band to the conduction band. In contrast, MOChas exhibit semiconducting behavior, positioning them as intermediates between conductive and insulating materials. For semiconductors, only *some* electrons have sufficient energy to transfer up to the conduction band, and their conductivity varies with temperature. Band dispersiveness also indicates electron mobility, where dispersive bands signify higher mobility and flatter bands indicate more localized electrons. High-symmetry k-paths to visualize these bands are taken along the Brillouin zone–a Voronoi-decomposed primitive cell of the reciprocal lattice. The electronic band structure diagram helps to visualize all of these parameters.

An input charge density is used from the SCF calculation to start DOS and band structure calculations. For either electronic structure calculation, an electronic loop precision of 1e-6 eV and an ionic loop precision of 1e-4 eV are used. Memory-conserving symmetrization of the charge density is used with no update of the crystal structure. Gaussian smearing is turned on with a width of 0.03 eV, and the atomic positions are the only ionic degrees of freedom. High-symmetry k-paths are chosen using the Setyawan-Curtarolo method [27] according to the space group of the lattice. To obtain the DOS for a given charge density or the eigenvalues for band structure plots, the input is read from the charge density (CHGCAR) file. The Wigner-Seitz radius for each atom type is ignored and lm-decomposed quantum numbers are written. Specifically for a DOS calculation, 2000 defines the number of electronic DOS grid points.

The DOS are normalized prior to plotting in order to adequately compare systems that have varying numbers of atoms. Both the DOS and band structure diagrams are plotted with Python Materials Genomics (Pymatgen) software [28], with a tolerance of 1e-8 eV to obtain the VBM and CBM in the band structure. Pymatgen may visualize band diagrams in such a way that the band structure appears to be indirect, rather than direct. When considering minima and maxima along band edges, the differences between candidate band minima (or between candidate band maxima) may be almost negligible. Here, we consider “negligible" as any difference that is smaller than 0.025 eV, or roughly room temperature. We choose this tolerance criterion because MOCha structures behave regularly at room temperature and are not normally treated at extreme temperatures. Algorithmically, Pymatgen may state that a band gap is indirect *numerically*, when in reality the minima points differ by very small amounts. In this case, when Pymatgen determines that a band gap transition is indirect, but the difference between minima or difference between maxima is smaller than 0.025 eV, we say that the band gap transition is "effectively direct".

Partial Charge Densities

The partial band-decomposed charge density can be used to analyze the contributions of different electronic orbitals or energy ranges to a specific region in real space. We select partial charge densities at the band gap, specifically at the VBM and CBM points. Consistent with the input WAVECAR file derived from the corresponding SCF calculation, symmetrization of the charge density is turned off completely. To obtain the partial charge densities at the band gap, the k-point and band index pair is selected that corresponds to the maximum energy level in the valence band, as well as the k-point-band index pair that corresponds to the minimum energy level in the conduction band. Partial band and k-point-decomposed charge densities are evaluated, and separated for all selected bands and k-points.

2.3 Modification of Structures

Inorganic-only structures

To further investigate the individual contributions of the inorganic structure, the isolated inorganic topologies are extracted and evaluated as separate entities from the MOCha. To construct the inorganic tubes, Pymatgen [28] is used to create code that truncates the chalcogen atom with a hydrogen in place of the ligand site, at the appropriate distance for each respective chalcogen-hydrogen single bond (1.46 Å for Se–H, 1.34 Å for S–H, and 1.65 Å for Te–H). The final lattice of the inorganic structure remains the same as that of its parent MOCha (Fig. 2.1A). High-symmetry k-paths are chosen using the Setyawan-Curtarolo method [27] according to the space group of the original MOCha lattice. A SCF calculation followed by a single-point band structure calculation were performed in order to obtain a band gap for each inorganic structure.

Hypothetical MOChas

Constructing hypothetical MOChas is crucial to evaluating experimental MOChas in this work, and is achieved through the help of Rhinoceros® architecture software. We begin with an inorganic template derived from experimentally-realized MOChas. All desired atomic species that compose the organic ligands are removed using Pymatgen [28], creating an inorganic backbone with a carbon skeleton guide that provides the coordinates to which the new ligands can be oriented (Fig. 2.1B, left panel). A one-to-one mapping is used to transform each atomic species into a unique HEX color code, and the atomic coordinates and HEX colors are converted into xyz inputs for Rhino, creating a skeleton file. Note that the atomic bond lengths (Å) can easily be scaled into the Cartesian coordinate system (mm) in Rhino, and vice versa. Next, the SMILES string of the desired ligand is constructed using Avogadro [29], optimized with the MMFF94 force field [30], and then imported as an xyz file for Rhino using the same methods to import the skeleton (Fig. 2.1B, middle panel). The orient3D command in Rhino helps to translate and rotate the new ligand into the desired carbon skeleton (Fig. 2.1B, middle panel). The points of this skeleton file with oriented new ligands are then exported, and the one-to-one mapping of HEX colors to atomic species helps to recover the hypothetical MOCha (Fig. 2.1B, right panel). This hypothetical

MOCha geometry can then be evaluated and relaxed as with experimentally-realized MOChas.

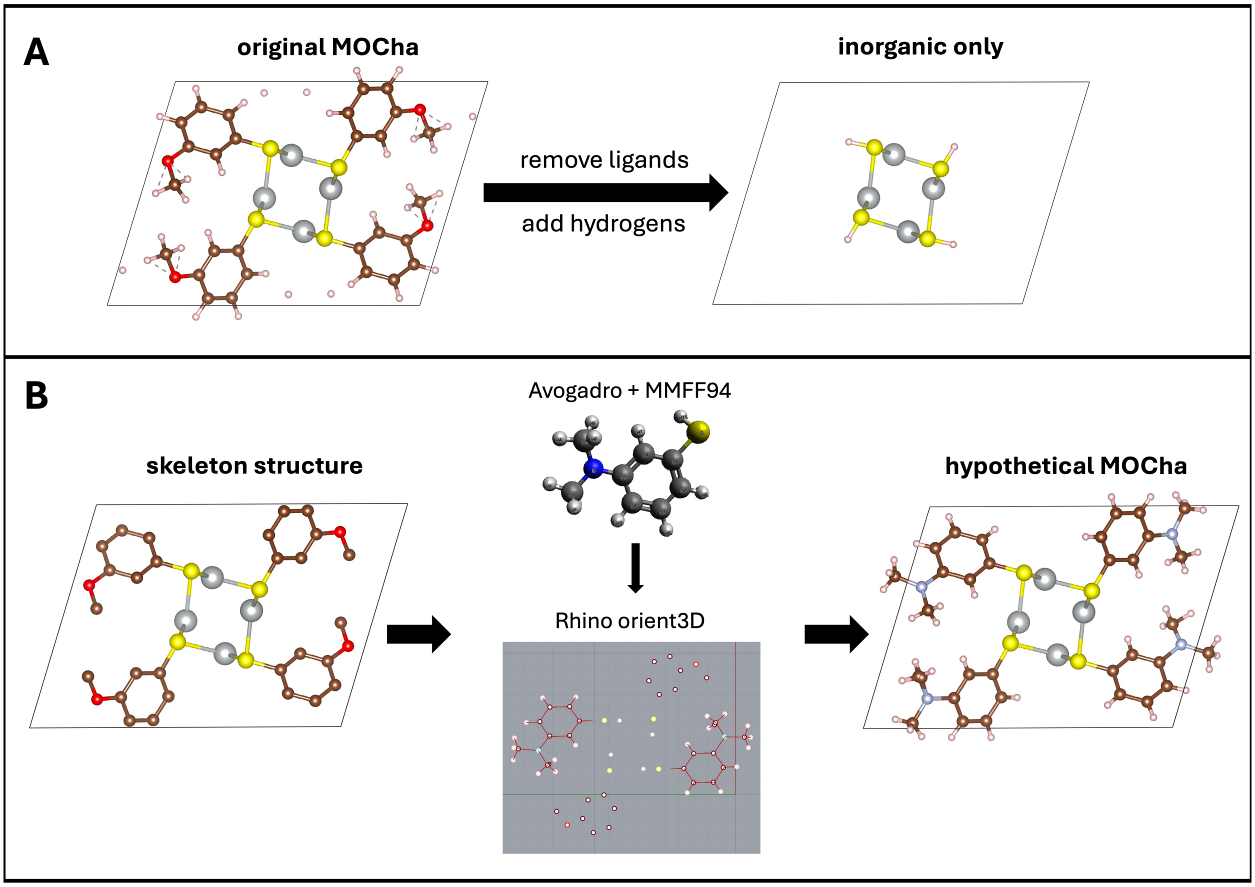
A
original MOCha
remove ligands
add hydrogens
inorganic only
B
Avogadro + MMFF94
skeleton structure
hypothetical MOCha
Rhino orient3D

Figure 2.1: **(A)** Procedure for constructing the inorganic only, in which atomic species that make the ligand are removed and the ligand is replaced with a hydrogen. **(B)** Procedure for creating a hypothetical MOCha.

Chapter 3

Don’t Sugar Coat it..or do...

The work described in this chapter is in preparation for submission as Ref. [31].

3.1 Introduction

It has been a long-standing hypothesis that atomic displacements induced by ligand selection are related to optical phenomena in the systems, and recently there have been reports of a variety of largely achiral, petroleum-derived organic ligands with aprotic functionalities (e.g. functional groups such as methoxy, methyl ester, and the halogens) [32, 33, 34, 35]. Hybrid materials incorporating chiral organic ligands can enable unique functionalities, including circularly polarized luminescence (CPL) [36, 37, 38, 39, 40]. Carbohydrates are biologically derived, highly-protic molecules that are amenable to derivatization with sulfhydryl groups, and so they present compelling targets for examining structure-function relationships across a series of chemically similar, chiral ligands.

We have taken advantage of recent developments in serial microcrystallography to determine MOCha structures. This study focuses on thiocarbohydrates, specifically the epimers 1-β-D-glucosethiol (compound **1**) and 1-β-D-galactosethiol (compound **2**). These sugar ligands precipitate with silver ions to form microcrystals of silver(I) thioglucose dihydrate and silver(I) thiogalactose dihydrate. Dehydration is reversible and yields silver(I) thioglucose monohydrate (compound **3**) and anhydrous silver(I) thiogalactose (compound **4**). Structures of these four microcrystalline samples were determined by small-molecule serial femtosecond crystallography (smSFX) at X-ray free electron laser (XFEL) facilities (LCLS and SACLA). Each compound forms a 1D MOCha structure with intense blue or green luminescence, and we show structural relationships for the resulting photophysical phenomena. Previously, 1D MOChas have been reported with yellow to orange fluorescence. Importantly, the difference of the hydroxyl position in the glucose and galactose derivatives resulted in entirely different inorganic connectivities for the two structures. We show that the inorganic centers are themselves chiral in both compounds, and the emission is circularly polarized. DFT modeling revealed that the dehydration in the galactose MOCha system is energetically more favorable than the glucose MOCha system, predicting reversible dehydration in glucose-based MOChas and irreversible dehydration in galactose-based MOChas. The optical shift is attributed to atomic displacements in silver thioglucose during water release/uptake, altering the electronic structure and energetics. These findings highlight structure-property relationships that may extend to other bioinorganic systems and offer promise for applications such as 3D displays, spintronics, and cancer diagnostics [6, 7, 8], due to their chirality, biocompatibility, and biofunctionalization potential [9, 10].

3.2 Methods

Two sets of relaxations are performed. First, a relaxation is carried out using selective dynamics on the hydrogens only, such that all other species in the system as well as its unit cell remain the same as the original experimental structure. Then, a full relaxation on all atoms in the system is performed without relaxation of the unit cell to eliminate computational caveats on energetics that may be sensitive to unrelaxed atoms. The k-point grid is based on the reciprocal lattice vectors, such that the number of subdivisions in each lattice direction $N_1,\ N_2,\ N_3 \approx |\mathbf{b}_1| : |\mathbf{b}_2| : |\mathbf{b}_3|$. Finally, self-consistent field (SCF) calculations are computed on the relaxed structures to provide a proper input charge density for electronic structure calculations. More information on the relaxation, SCF, and electronic structure calculations is reported in Section 2.2.

We evaluate the energetic favorability of the dehydrated systems by performing a SCF calculation on the **3** and **4** MOChas and compare the resulting final energies of the experimentally-dehydrated systems with those of computationally-dehydrated systems. Computational dehydration is achieved by taking the final relaxed structures of **1** and **2** and removing water from the systems such that the final computationally-dehydrated structure matches the stoichiometry of the experimentally dehydrated structures **3** and **4**. Fig. 3.1 demonstrates the process of computational dehydration for the glucose MOCha system. 2 waters are removed computationally from compound **1** and 3 waters from compound **2**. The energy difference from the experimentally-dehydrated to the computationally-dehydrated structure per formula unit is then compared, in which the dehydrated structure whose energy difference is more negative relative to its computationally-dehydrated counterpart is the structure that is more energetically favorable.

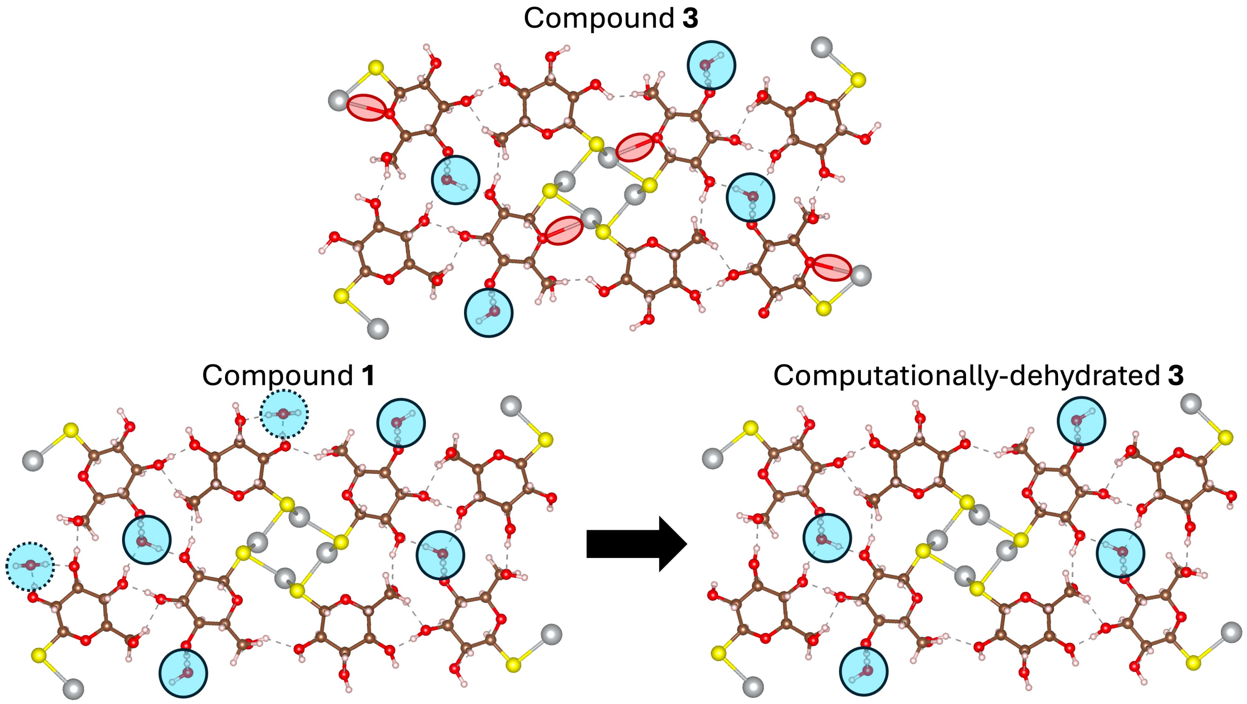

Figure 3.1: Computational dehydration process of sugar MOChas, shown here specifically for the glucose MOCha system. Blue solid-line circles encase water molecules, whereas blue dotted-line circles encase water molecules that will be dehydrated, i.e. "computational dehydration". Red solid-line ovals encase Ag-O bonds that are present in compound **3**, but not in **1**.

Since the stoichiometries of the final dehydrated structures no longer have the same formula units as the hydrated **1** and **2**, their total system energies cannot be divided and compared with one another. Instead, the interaction of water with the glucose and galactose MOChas can be evaluated using the equation:

$$E_{system} = \frac{aE_{hydrated} - bE_{dehydrated} - n_{(H_2O)}E_{(H_2O)}}{n_{atoms}} \tag{3.1}$$

where a and b are coefficients aligning the same atomic species ratio between the hydrated and dehydrated systems, $E_{hydrated}$ and $E_{dehydrated}$ are the total energies of the hydrated and dehydrated systems, respectively, $n_{(H_2O)}$ is the difference in the number of water molecules, $E_{(H_2O)}$ is the total energy of an isolated water molecule, and n_{atoms} is the total number of atoms in the hydrated system.

3.3 Results and Discussion

Crystal Synthesis and Structural Characterization by smSFX

An overview of the synthesis and product structures is shown in Fig. 3.2. Compounds **1** and **2** were synthesized in a one-step reaction by reacting glucosethiol or galactosethiol– a pair of epimers, each exhibiting five stereocenters and five hydroxyl groups– with silver nitrate at room temperature. Scanning electron micrographs (SEM) revealed needle-shaped crystals with diameters of a few hundred nanometers and lengths of several micrometers (Fig. 3.2B-C). Dehydration of **1** and **2** was achieved either thermally (at 90 °C for 24 hours) or by suspending the compounds in polar solvents such as ethanol, yielding dehydrated forms **3** and **4**; additional details will be reported later. Both **1** and **2** were dispersed readily in water, and these suspensions were prepared at a loading of 1–4 mg/mL for subsequent smSFX characterization. To obtain the respective dehydrated-form structures **3** and **4**, **1** and **2** were heated at 90 °C for 24 hours and then suspended in either ethanol or methanol.

All four MOChas are well-behaved samples for serial microcrystallography; they were routinely straightforward to collect data on and seldom did any issues like clogging arise. This is primarily attributed to the extremely polar surface environment of the crystals from the exposed hydroxyl groups of sugar ligands. The crystals themselves suspend well in any polar protic solvent we tried and did not appreciably clump or settle over our normal experiment timescales. Each XFEL experiment used a different sample delivery method. At LCLS we used droplet-on-tape and droplet-on-demand methods, where small volumes containing crystals were exposed to the beam, either dropped in air or carried on a belt to the interaction points. At SACLA, we used gas virtual dynamic nozzles having a 200-µm diameter. Details of the data collection and reduction methods can be found in Aleksich *et al* [41].

smSFX analysis revealed that all four compounds have a similar molecular formula, $C_6H_{12}O_5SAg$, but differ in the number of water molecules of hydration per unit cell (0–2). Glucose-based MOChas (**1** and **3**) and galactose-based MOChas (**2** and **4**) adopt hybrid organic-inorganic structures, featuring 1D inorganic nanowires composed of Ag and S atoms. These nanowires are surrounded by organic motifs derived from 1-β-D-glucose (**1**, **3**) and 1-β-D-galactose (**2**, **4**), respectively (Fig. 3.2D-G).

Compound **1** crystallizes in the orthorhombic crystal system and the $P2_12_12$ Sohncke space group, classifying it as a chiral material [37, 42, 43] (Fig. 3.2D). The rod-like motif for the inorganic nanowire has recently been reported for other 1D MOChas [44, 45, 4, 32]. Briefly, the AgS nanowire in **1** consists of repeating Ag_4S_4 units linked by four AgS bonds ranging from 2.519 to 2.526 Å, forming a 1D chain (Fig. 3.2D, Fig. B.1A). Each Ag_4S_4 unit contains a pyramidal Ag_4 subunit, where each silver atom is coordinated to two or three other silver atoms at different Ag-Ag distances from 3.121 to 3.369 Å (Fig. 3.2D, Fig. B.1B). Four glucosethiol ligands surround the Ag_4 pyramid, covering four of its faces. Notably, this subunit Ag_4 core is chiral when considered in isolation: it is not superimposable on its mirror image, even when setting aside the stereocenters on the organic ligands [42]. Similarly, compound **3** observed the same orthorhombic crystal system and $P2_12_12$ space group as **1** (Fig. 3.2F, Fig. B.2). However, the asymmetric unit of **3** contains only one water molecule, half the number found in **1** (Fig. 3.5D), reflecting partial dehydration.

Compound **2** crystallizes in a monoclinic Bravais lattice with a $P2$ Sohncke space group (Fig. 3.2E). Its AgS core features a unique double-helix structure, composed of twin AgS strands arranged helically. Interestingly, the dehydrated form of **2** (compound **4**) undergoes a transition from the $P2$ space group to the $C2$ space group within the same monoclinic system (Fig. 3.2G). Despite this change, the inorganic AgS nanowire remains a double-helix. The absence of water molecules in **4** indicates complete dehydration (Fig. 3.2G).

The primary differences observed between the AgS inorganic nanowires of the glucose MOChas and galactose MOChas systems stem from distinct hydrogen bonding patterns. In both systems, abundant OH$\cdots$O hydrogen bonds among ligands and water molecules create a supramolecular 3D structure. In the glucose MOChas system, hydrogen bonding predominantly occurs between chains. In contrast, the galactose MOChas system exhibits interchain and intrachain hydrogen bonds (Fig. B.3). Importantly, differences in the inorganic core give rise to variations in luminescence.

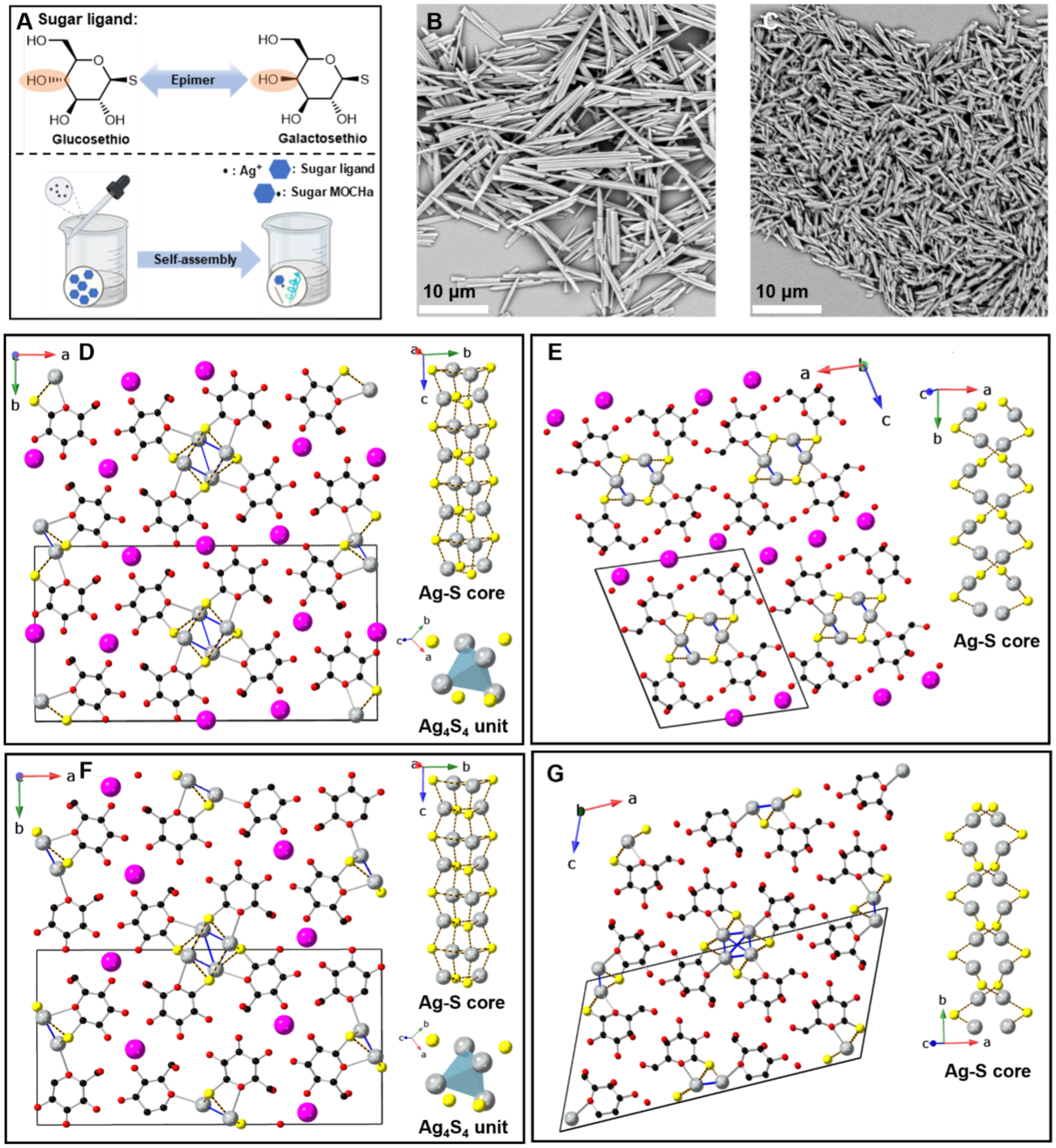
A
Sugar ligand:
HO
HO
HO
OH
O
S
Epimer
Glucosethio
Galactosethio
• : Ag⁺
: Sugar ligand
•: Sugar MOCha
Self-assembly
B
10 μm
C
10 μm
D
a
b
c
Ag-S core
Ag₄S₄ unit
E
Ag-S core
F
Ag-S core
Ag₄S₄ unit
G
Ag-S core

Figure 3.2: **(A)** Material design of chiral bioinorganic MOChas: multiple chiral, hydroxyl, and only one different stereocenter at carbon 4 (highlighted in orange oval) between glucosethio and galactosethio; the bottom panel illustrates sugar MOCha self-assembly via silver ions with sugar ligands. **(B-C)** Scanning electron micrographs (SEM) of both silver (I) thioglucose dihydrate (**1**) and silver (I) thiogalactose dihydrate (**2**), respectively. **(D)** Crystal structure of silver (I) thioglucose dihydrate (**1**). **(F)** Crystal structure of silver (I) thiogalactose dihydrate (**2**). **(E)** silver (I) thioglucose monohydrate (**3**). **(G)** Crystal structure of anhydrous silver (I) thiogalactose (**4**). Color code: Ag, silver; S, yellow; O, red; C, black; Water, purple. Hydrogen atoms have been omitted for clarity.

Spectroscopic Characterization

Powdered crystals were prepared for photoluminescence (PL) emission measurements and UV-Vis absorption (Fig. 3.3A). Notably, the **1** and **2** under UV light excitation exhibit intense blue and green photoluminescence, respectively, consistent with the hypothesis that distinct inorganic nanowires result in different luminescence (Fig. 3.3A). The **1** showed a broad emission band peaking at 483 nm with an absorption band around 330-380 nm, whereas the **2** exhibited a similar broad emission band centered at 507 nm along with a 250-320 nm absorption band. Importantly, both **1** and **2** exhibit a relatively large Stokes shift, suggesting the possible involvement of a self-trapped exciton luminescence mechanism [46].

The quantum yield (QY) of compound **1** in deionized (DI) water at room temperature is 13.41%, while that of compound **2** is slightly higher at 15.57%. These values are higher than most of the 1D AgS-based MOCha family, likely due to the Ag-O interaction observed in the structures (Fig. B.4). Additionally, interchain and interchain H-bonds facilitate numerous non-covalent interactions. This interlocked hybrid inorganic-organic system might help to suppress non-radiative decay [47]. Time-resolved PL (TRPL) decay was well-described by a bi-exponential function, with a fast prompt and slow dominant decay process. It is important to note that **1** exhibits PL lifetimes extending to hundreds of nanoseconds. In contrast, compound **2** has a much shorter extracted lifetime of approximately 21 ns. This distinct lifetime may be attributed to their inorganic structures, leading to different electronic structures.

Considering the chirality of these AgS chains from their crystallographic structures and bright photoluminescence, we examined the chirality of the samples by circular dichroism (CD) and CPL of both **1** and **2** in dilute DI water suspension (Fig. 3.3C-E). The resulting CD spectra reveal that **1** and **2** display bisignate shapes with signals at 219 and 323 nm, and 248 and 278 nm, respectively. These signals differ from those of the corresponding D-glucose and D-galactose [48], indicating that the CD profiles of **1** and **2** do not arise solely from the organic motif. Notably, **1** showed CPL centered at 483 nm (Fig. 3.3D), which is rare for 1D materials. The dissymmetry factor of emission was calculated to be 5.8×10^3, a modest yet significant value compared to other metal-organic hybrid material emitters. A similar phenomenon was observed for **2**, with a dissymmetry factor of 2.2×10^3 (Fig. 3.3E). In contrast, as expected, the achiral control sample, silver(I) methyl 2-mercaptobenzoate (2MMB), showed no detectable CD and CPL (Fig. 3.3C, 3.3F), validating our hypothesis that the chiral sugar ligands induce a chiral inorganic core, resulting in CPL activity [37, 43]. Therefore, CPL activity is intrinsic to these chiral silver-based MOChas. The consistency between the CPL and PL spectra, along with the well-defined crystallographic structure, helps us understand the intrinsic optical activity of the infinite chiral AgS inorganic network. To the best of our knowledge, this work reports the first examples of chiral ligand-induced chiral inorganic structure, leading to optical asymmetry in the MOChas family.

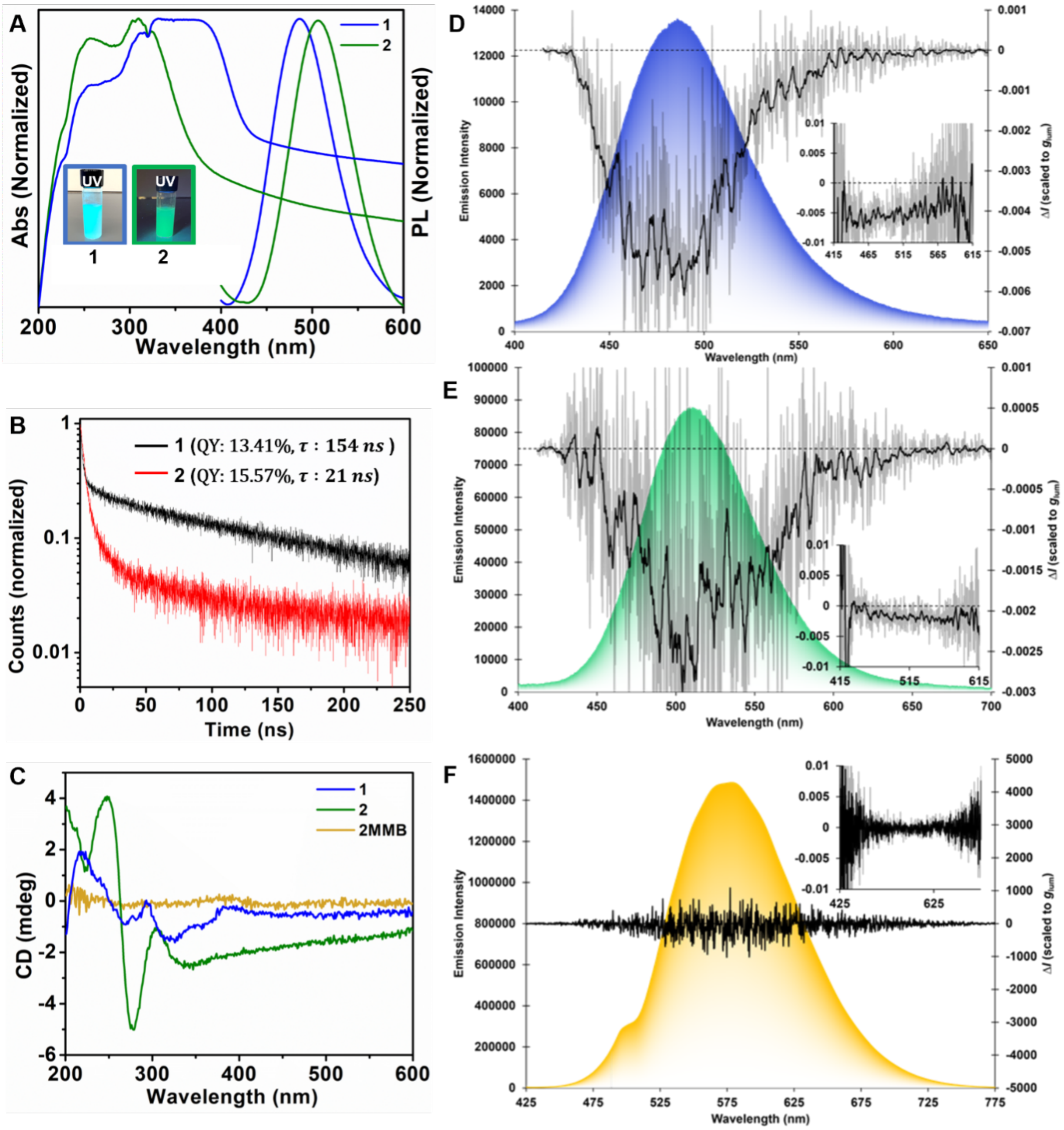

Figure 3.3: Optical properties of **1** and **2**. **(A)** Absorption and PL spectra of **1** and **2** at room temperature. The photographs of **1** and **2** under UV light are shown in the inset: **1** is highlighted in a rectangular blue frame, and **2** is highlighted in a rectangular green frame. **(B)** Time-resolved PL decays of **1** and **2** along with the decay. **(C)** circular dichroism (CD) spectra for **1**, **2**, and the control sample 2MMB, respectively. **(D-F)** CPL spectra of **1**, **2**, and the control sample 2MMB were excited at 350 nm, respectively.

DFT Modeling of the Electronic Structure

To understand the electronic origin of trends in the optical properties of the four MOChas, DFT calculations are performed. Across all systems, the AgS inorganic core dominates the electronic structure at both the valence band maximum (VBM) and the conduction band minimum (CBM), with minimal contributions from the ligands, emphasizing the AgS core's central role in emission and electronic behavior. Furthermore, inorganic electron orbitals in the VBM are also highly localized, which can be observed from Fig. B.5.

The left panel of Figure 3.4A shows the calculated band structure of **1**, featuring an effectively direct band gap of 2.240 eV at the Γ point with relatively flat bands surrounding this point, indicating low electron mobility. The Brillouin zone inset shows the k-paths, in which the $\Gamma-$Z path corresponds to the plane perpendicular to the inorganic 1D tube, and $\Gamma-$X is the path along the 1D tube. The band structure showcases flatter bands along $\Gamma-$Z and far more dispersive bands along $\Gamma-$X, indicating more electron mobility along the 1D AgS inorganic core. The density of states (DOS) shows that the VBM and CBM are primarily located on the AgS core (middle panel in Fig. 3.4A), suggesting that the AgS inorganic nanowire contributes to photoluminescence. In the conduction band (Fig. 3.4A, rightmost panel), the diagram exhibits electron delocalization. Overlapping lobes of Ag(d) orbitals and polarized inner lobes of S(p) orbitals contribute to central electronic overlap–notably, cross-pairs of Ag(d) orbitals alternate between the central electronic overlap. Additionally, weak interactions between the C^1 atom's C(p) orbital in the aliphatic ring and the neighboring S(p) orbital are observed. Parallel pairs of Ag(d) orbitals and a parallel single-lobe pair of Ag(d) orbitals contribute to central electronic overlap.

Interestingly, the band structure of **3** in Fig. 3.4C reveals another effectively direct band gap of 2.214 eV at the Γ point. Note that the band structure and Brillouin zone k-path of **1** (Fig. 3.4A) and **3** (Fig. 3.4C) are indeed quite similar, differing in band gap width by merely 0.026 eV. The $\Gamma-$Z and $\Gamma-$X paths in the Brillouin zone indicate k-paths perpendicular to and along the tube, respectively. Similar to **1**, the $\Gamma-$Z path of **3** features very flat band edges, whereas the $\Gamma-$X path along the tube features very dispersive bands, indicating higher electron mobility in these regions. Additionally, at the CBM, weak interactions between the C^1 atom's C(p) orbital in the aliphatic ring and the neighboring S(p) orbital are observed (Fig. 3.4C, right panel). Similar to compound **1**, in the conduction band of compound **3**, all Ag(d) orbitals are highly delocalized and polarized inner S(p) lobes contribute to central electronic overlap. This participation of all Ag(d) orbitals in the central electronic overlap in **3**, as opposed to the two opposing pairs in the hydrated **1**, may result in higher stability and therefore red-shifted color of the partially dehydrated glucose structure **3**. Additionally, weak interactions between the C^1 atom's C(p) orbital in the aliphatic ring and the neighboring S(p) orbital are observed.

In contrast, **2** is the only MOCha in this series that exhibits an indirect band gap of 2.974 eV between the VBM at the (0.000, 0.530, 0.463) point and the CBM at the Z wave vector (left panel in Fig. 3.4B). The $\Gamma-$Z and $\Gamma-$Y k-paths indicated from the Brillouin zone (Fig. 3.4B, middle inset) showcase dispersive bands along and flat bands perpendicular to the tube, respectively. Minimal band dispersion at the band gap suggests weak orbital hybridization between adjacent AgS helices, contributing to localized charge carriers and a slightly higher PLQY compared to **1**. DOS analysis highlights the role of the AgS core in determining the band gap, while organic ligands influence emission color (middle panel in Fig. 3.4B). In **2**, Ag(d) orbitals are smaller than S(p) orbitals and remain localized in the VBM (Fig. B.5B). Slight delocalization occurs in neighboring C(p) orbitals within the aliphatic ring and O(p) orbitals. In the CBM, all four Ag(d) orbitals participate in central delocalization, while S(p) orbitals lack polarization (right panel in Fig. 3.4B).

For **4**, the band structure (Fig. 3.4D, left diagram) features an effectively direct band gap of 2.387 eV at the N wave vector, primarily shaped by the AgS structure. The $\Gamma - \mathrm{Z}$ and $\Gamma - \mathrm{N}$ paths from the Brillouin zone inset indicate the *k*-paths perpendicular to and along the inorganic 1D core, respectively. The $\Gamma - \mathrm{N}$ path in the VBM features more dispersive bands than in the CBM, indicating more electron mobility. The CBM exhibits electron delocalization across all four Ag(d) orbitals. One cross-pair of S(p) orbitals lacks polarization, whereas the remaining cross-pair forms distorted crescent shapes around the sulfur atom, suggesting orbital hybridization (Fig. 3.4D, right panel).

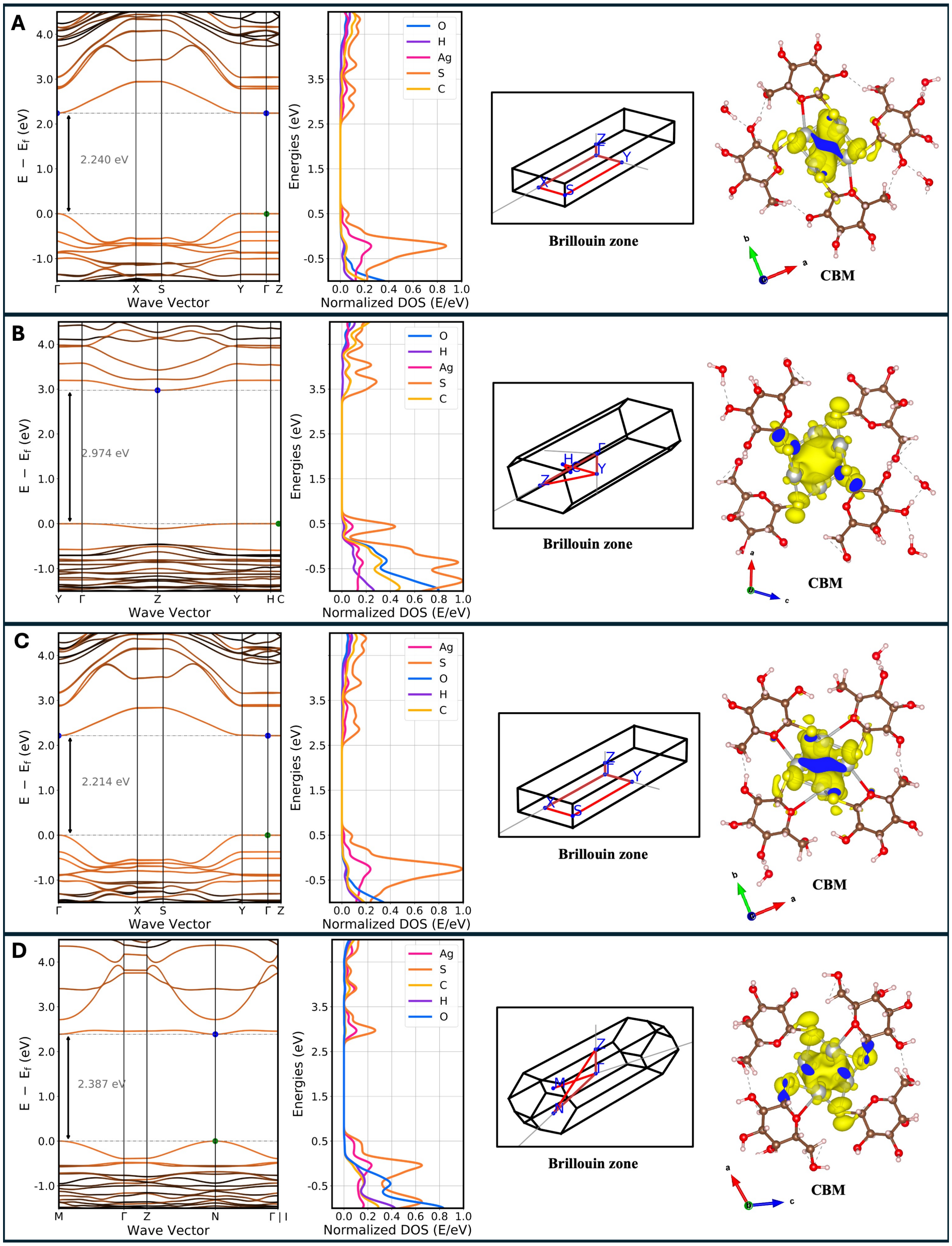

Figure 3.4: **(A-D)** Electronic structure of compounds **1-4**, respectively. For each structure, the left inset shows the band diagram, where orange bands represent inorganic interactions, black bands represent organic interactions, and interpolated colors indicate mixed inorganic-organic interactions. Blue and green points highlight the wave vectors at which the CBM and VBM occur, respectively. The middle panel presents the density of states (DOS), separated by atomic species. The middle inset displays the Brillouin zone *k*-path for the visualized band structure. The right panel displays partial charge densities at the CBM for each compound, with some other parts of the unit cell and water molecules omitted for clarity. Note that figures with a larger number of bands correspond to MOChas with a larger number of atoms.

Energetic Favorability and Kinetic Dehydration/Rehydration

Understanding the processes that govern hydration and dehydration is a critical aspect of materials science [49]. Exploring the structural and electronic changes of bioinorganic MOChas **1-4** induced by water release and uptake provides insights into their properties and applications. Heating **1** in a vacuum oven at 90 °C for 24 hours resulted in 50% water loss, producing partially dehydrated **3**, as confirmed by TGA, in line with their asymmetric unit (Fig. 3.5A, 3.5D). PXRD analysis revealed the disappearance of the first diffraction peak in **3** compared to **1**, indicating structural distortion. Remarkably, rehydrating **3** restored its PXRD pattern to that of hydrated **1** (Fig. B.6). Based on these observations, we conclude that the hydration and dehydration processes are reversible. To investigate the kinetics of water release and uptake in the glucose MOCha system, we conducted fluorescence measurements during the dehydration and rehydration processes. Fig. 3.5B-C illustrates the kinetics of the color shift between blue-luminescent **1** and green-luminescent **3** over time. The chromogenic nature of water uptake and release provides a convenient visual excitonic readout of the crystal's hydration state. Structural distortions in the AgS core, as highlighted by red circles in the AgS nanowires (Fig. 3.5D), suggest that water release/uptake induces distortion in the nanowire structure, modulating the electronic properties and resulting in altered luminescence. Interestingly, TGA, PXRD, and PL data indicated an irreversible solid-solid transformation from **2** to **4**, with no change in emission frequency (Fig. B.7). However, UV-vis spectra revealed a broader absorption band for **4** compared to **2**, likely due to variations in the Ag-Ag inorganic network (Fig. B.8).

Water release and uptake are reversible in the glucose MOCha system but irreversible in the galactose MOCha system, prompting an investigation of the energetic favorability for these processes using DFT calculations. To understand the hydration and dehydration process of the compounds, we perform a DFT energetic comparison between glucose-based MOChas and galactose-based MOChas. Compound **2** has a formula of $(AgSC_6H_{11}O_5)_4$ and **1** has a formula of $(AgSC_6H_{11}O_5)_8$, making them the proper ratio (i.e. same formula unit) to compare energetics per formula unit as calculated by DFT. First, a self-consistent field (SCF) calculation is performed on the fully relaxed structure. Then, the total energy of the system obtained from the SCF calculation is divided by the total number of formula units in the MOCha, that being 4 formula units for the MOCha **2** and 8 for the MOCha **1**. The MOCha that has the most negative energy per formula unit is the structure that DFT predicts to be more energetically favorable when hydrated. Performing energetics analysis revealed that **1** is 0.224 eV lower per formula unit than its **2**, suggesting that the hydration of the glucose MOCha is more energetically favorable than that of its galactose counterpart.

Since the stoichiometries of the partially-dehydrated **3** and fully-dehydrated **4** no longer have the same formula unit, their total system energies cannot be compared with one another. Instead, we achieve analysis of the isolated structures by creating computationally dehydrated **3** and **4** (Fig. 3.1), in which the compound that is more negative per formula unit relative to its computationally-dehydrated counterpart is the dehydrated structure that is more energetically favorable. Energetics analysis revealed that the experimental **4** is 0.257 eV per formula unit lower than the computationally-dehydrated **4**, whereas the experimental **3** is 0.101 eV per formula unit lower than the computationally-dehydrated **3**. Because the difference between experimental and computational **4** is greater, this means that dehydration of **4** is more energetically favorable than that of **3** and validates the irreversible hydration that occurs in the galactose MOCha system.

Another way to model the interaction of water with the sugar MOChas is via Eq. 3.1, the dehydration of the system. The atomic ratio is 1:1 for hydrated to dehydrated states in the glucose MOCha system and 2:1 in the galactose MOCha system. In the galactose MOCha, three water molecules are removed during dehydration, whereas the partial removal of two water molecules occurs in the glucose system. The total number of atoms in **1** is 210, whereas the total number of atoms in **2** is 105, yielding the following equations:

$$\frac{E_{\mathbf{1}} - E_{\mathbf{3}} - 2E_{H_2O}}{210} \tag{3.2}$$

$$\frac{E_{\mathbf{2}} - \frac{1}{2}E_{\mathbf{4}} - 3E_{H_2O}}{105} \tag{3.3}$$

From the above equations, the galactose system has a final energy per atom of -0.01 eV and the glucose system has a final energy per atom of -0.008 eV. These energy differences between hydrated and dehydrated structures are quite small, indicating that there is a low energetic barrier to overcome for dehydration to be possible. This aligns with experimental results, in which the dehydrated structures **3** and **4** can be obtained by simply heating the hydrated forms **1** and **2** to 90° C for 24 hours. Overall, changes in luminescence are attributed to nano-inorganic structural distortions induced by water release and uptake, which modulate the electronic structure and energetics of the MOChas.

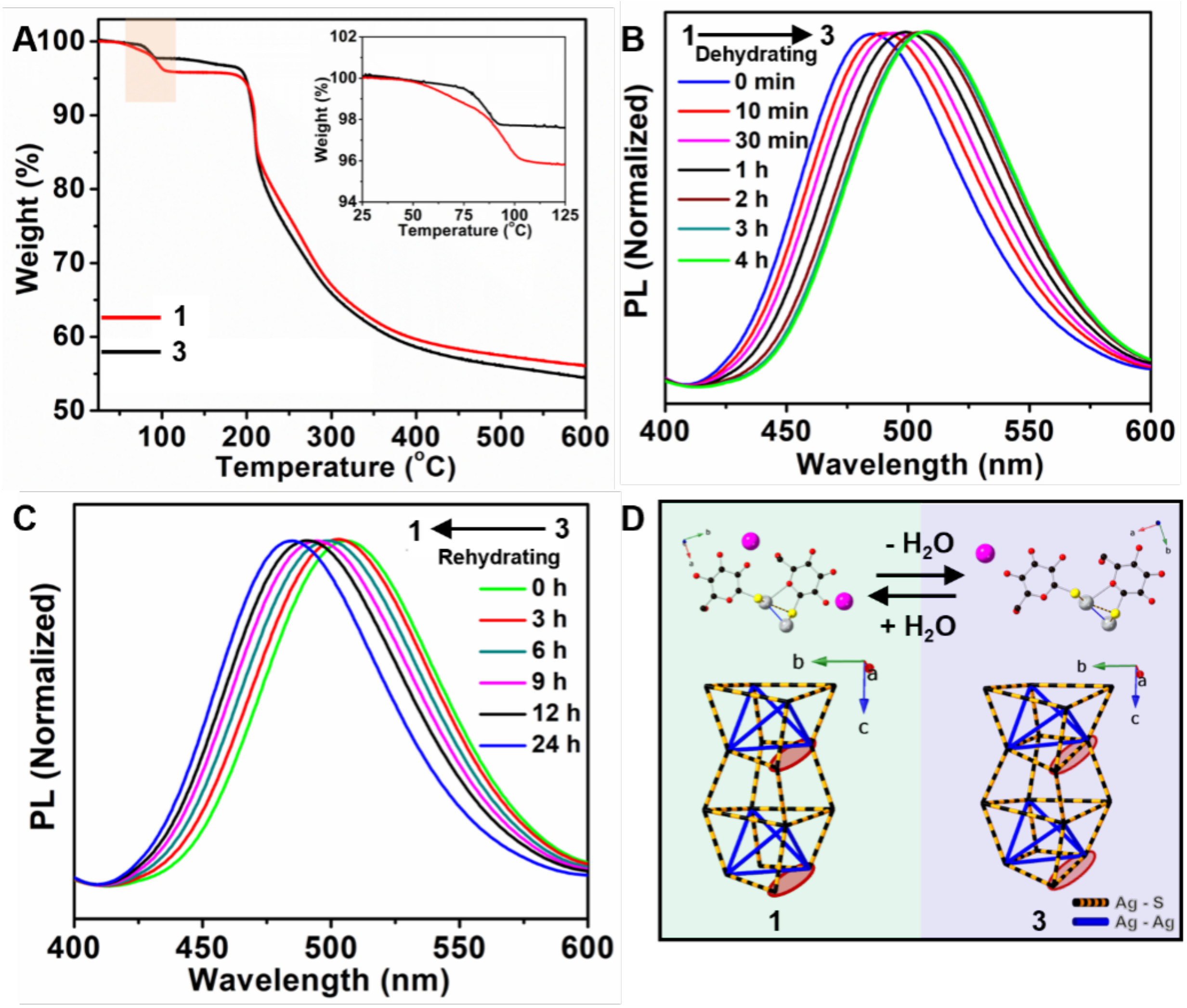

Figure 3.5: Kinetic uptake/release of water in glucose MOCha system. **(A)** TGA curves of glucose MOCha **1** and **3**, with a zoom in the inset. **(B)** Emission spectra show the chromogenic transition of initial **1** from blue to green **(3)** during dehydration in ethanol solvent (1 mg/2 mL). **(C)** Emission spectra show the chromogenic transition of initial **3** from green to blue (1) during rehydration in water solvent (1 mg/2 mL). **(D)** Comparison between **1** (left panel, highlighted in green) and **3** (right panel, highlighted in purple), focusing on the asymmetry unit (upper panel) and AgS network (lower panel).

3.4 Conclusion

In summary, bioinorganic glucose and galactose MOChas with PLQY were synthesized using a pair of epimeric ligands. A comprehensive XFEL diffraction analysis revealed 1D and richly hydrogen-bonded structures of four bioinorganic MOChas. Our study provided detailed insights into distinct chiral inorganic AgS arrangements. This enabled us to achieve the first experimental MOChas with optical asymmetry and report the chiral inorganic structure that induces CPL in MOChas. The glucose-based MOCha demonstrated a reversible dehydration/rehydration process, leading to a reversible readout of color shift between green and blue. In contrast, the galactose MOCha underwent an irreversible water release.

Dehydration/rehydration alters the distortion of the inorganic core between the hydrated and dehydrated states of MOChas. This work establishes a foundation for developing MOChas with optical asymmetry, linking water release and uptake in crystalline materials to their optical dynamics and potential applications in excitonic readout. Furthermore, the work presented in this chapter is part of a broader effort to understand the origins of fluorescence (emission color) in various 1D MOChas. Coupling DFT and experimental analysis, we hope to unveil the origins of emission colors by analyzing properties such as the HOMO-LUMO gap of the participating ligand, metallophilic interactions, electronic properties, and distortion present within the inorganic structure.

Chapter 4

Functional Group Drivers and Silver MOCha Passenger Princesses

The work described in this chapter is in preparation for submission as Ref. [50].

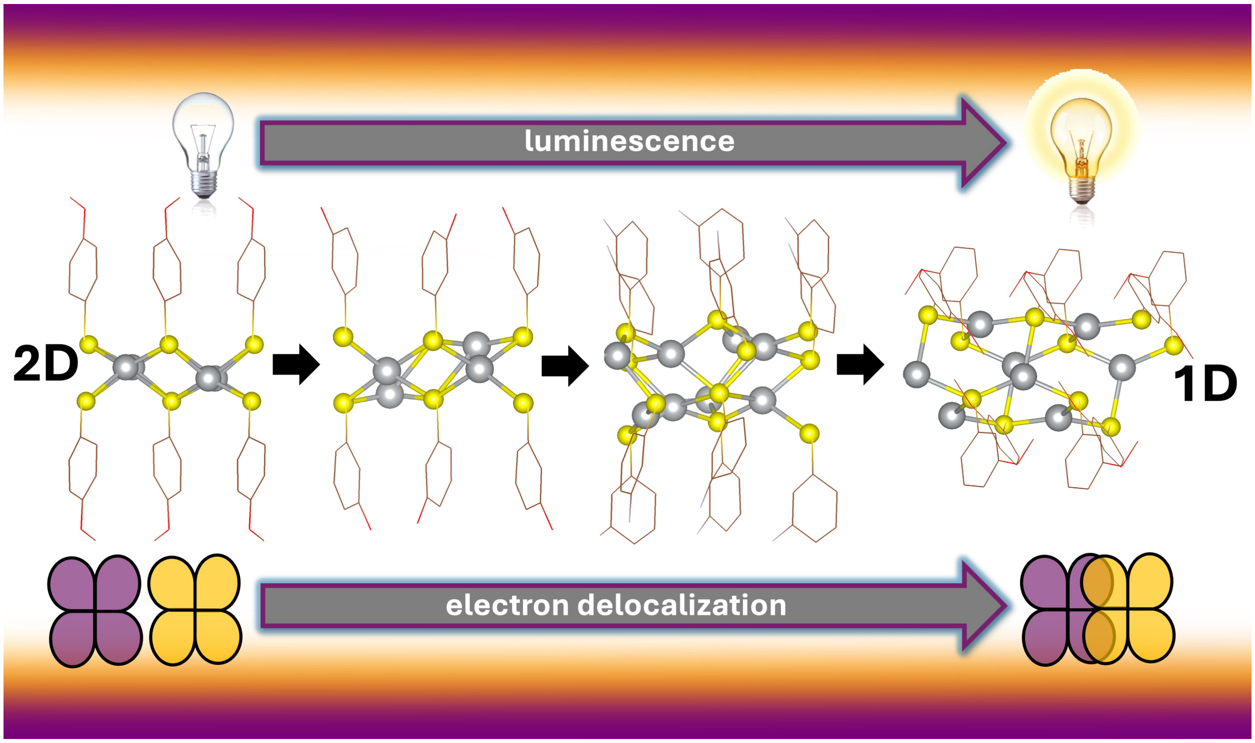

Figure 4.1: Graphical abstract showcasing the structural, luminescent, and electronic trends across silver benzenethiolate MOCha series.

4.1 Introduction

The coinage metals within the MOCha class of materials possess a range of coordination modes and self-assembling properties. Steric hindrance of the ligands via functional group position or ligand shape consequently affects the resulting inorganic structure of the MOCha [33, 32, 51], and therefore its electronic and luminescent properties [52, 53, 54, 55]. The flexibility and variability in MOCha composition means that we can deliberately tune the properties of MOChas via organic ligand selection [55].

In this work, we report the electronic, structural, and luminescent properties of silver benzenethiolate (AgSPh-X) MOChas, where X denotes the functional group and position around the phenyl ring of the ligand. Here, we indicate position interchangeably between numerical and chemical nomenclature: the 4- position is *para* (p), and the 3- position is *meta* (m). Specifically, we observe a 2D MOCha silver 4-methoxybenzenethiolate (compound **1**, AgSPh-p-OCH_3), a 1D MOCha 3-methoxybenzenethiolate (compound **4**, AgSPh-m-OCH_3), and two topologically distinct MOChas– 3-hydroxythiophenolate (compound **2**, AgSPh-m-OH) and 3-aminothiophenolate (compound **3**, AgSPh-m-NH_2)– that capture the range between 2D and 1D structures. The experimental procedure for the MOChas based on the isomeric methoxy series (compounds **1** and **4**) is described in Ref. [55].

We find that the ligand functional group X plays a critical role in determining the topology of silver benzenethiolate MOChas. However, while the functional groups drive the structural formation of these MOChas, they do not explicitly participate in the resulting electronic structure properties. To demonstrate that compounds **2** and **3** are interpolations of the possible series of distortions across 2D to 1D topologies, we create hypothetical 2D and 1D AgSPh-X MOChas for the 3-aminothiophenol (m-NH_2) and 3-hydroxythiophenol (m-OH) ligands using inorganic AgS templates that were derived from experimentally-realized MOChas **1** and **4**. Performing density functional theory (DFT) self-consistent field calculations on the relaxed geometries of the hypothetical m-NH_2, m-OH, and experimental **2**,**3** reveals that compounds **2** and **3** are energetic intermediates between the 2D and 1D prototypes. Furthermore, DFT-based electronic structure calculations of compounds **1**-**4** demonstrate that trends in the electronic band gap, electron orbital delocalization at the conduction band, and luminescence across the AgS series support the progression from 2D to 1D inorganic dimensionality.

4.2 Methods

All atomic species in the structures were allowed to relax while the unit cell volume and lattice parameters remained constant. Self-consistent field (SCF), density of states (DOS), and band calculations are then performed on the relaxed geometries. More information on the relaxation, SCF, and electronic structure calculations can be found in Ch. 2.2.

To confirm that the ligand functional group X plays a critical role in determining the topology of the resulting MOCha, we create hypothetical 2D and 1D AgSPh-X MOCha prototypes for the functional groups m-NH_2 and m-OH using Rhino. The inorganic AgS templates are derived from experimentally-realized MOChas, namely AgSPh-p-OCH_3 for the 2D template and AgSPh-m-OCH_3 for the 1D case. The ligands present in AgSPh-m-NH_2 and AgSPh-m-OH, respectively, were then attached computationally to the 2D and 1D templates to create prototype models. More details to this method are described in Ch. 2.3. After relaxing, a self-consistent field calculation was performed on the 2D, experimental, and 1D models for m-NH_2 and m-OH. Inorganic-only band structure diagrams are then obtained and evaluated using methods also described in Section 2.3.

4.3 Results and Discussion

Experimental Details

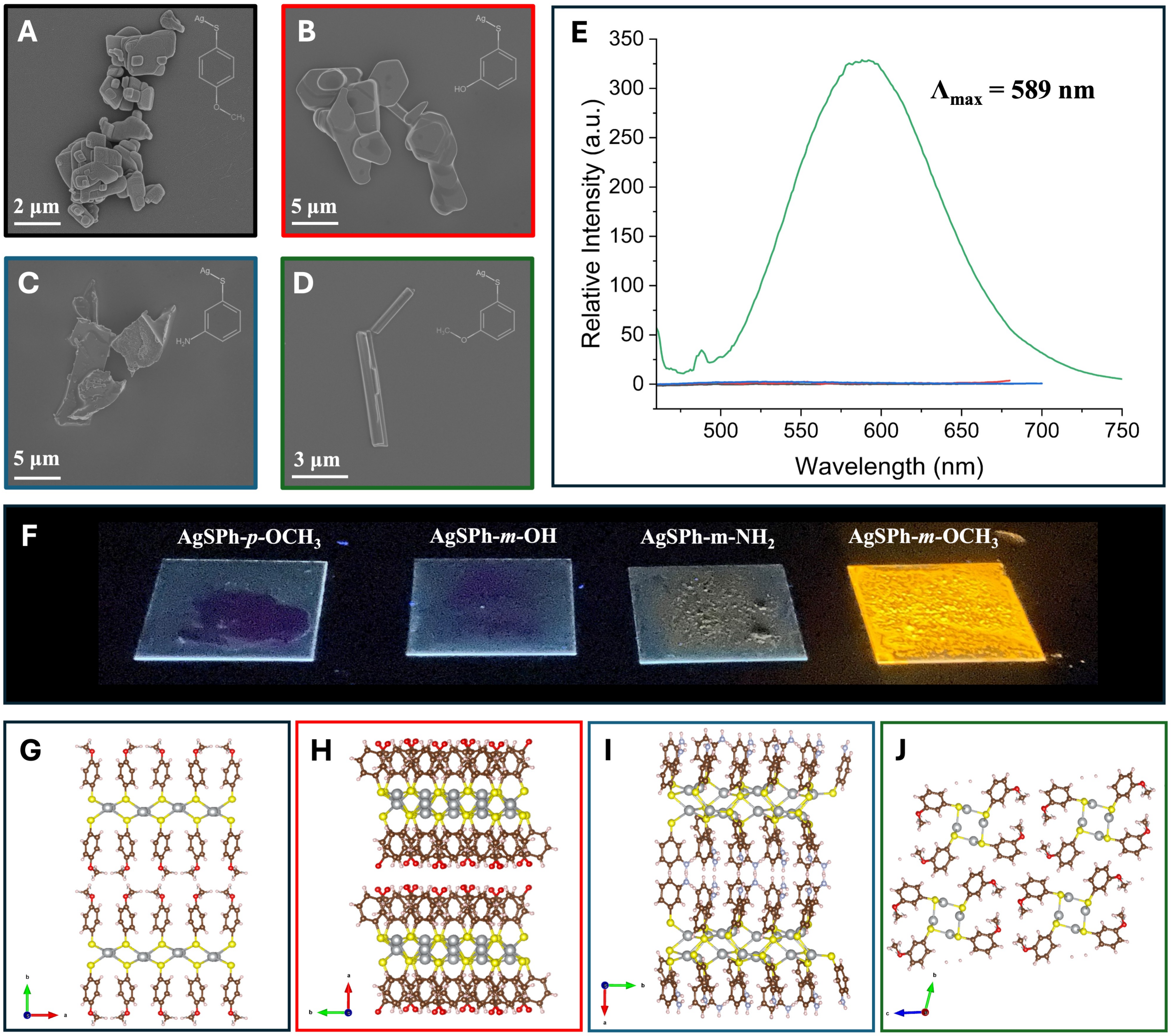

Figure 4.2: **(A-D)** Example morphologies of compounds **1-4**, with the ligand inset. **(E)** Normalized emission spectra of the four MOChas. Compound **4** is the only photoluminescent MOCha with a maximum emission peak at 589 nm. **(F)** Solid-state powder samples of compounds **1**–**4** illuminated with ultraviolet light. **(G-J)** Resolved structures for compounds **1-4**.

Scanning electron micrographs (SEM) of the MOChas are collected in Fig. 4.2A-D and reveal distinctive habit differences depending on the position and type of the functional groups on the phenyl ring. Notably, the *para* position of the methoxy species results in flat basal planes with step edges for compound **1** (Fig. 4.2A). Such visuals are less prominent in compounds **2** and **3** (Fig. 4.2B-C), which feature functional groups at the *meta* positions. Conversely, placing the methoxy functional group at the *meta* position in the ligand produces needle-like crystals for compound **4** (Fig. 4.2D). All MOCha product sizes are quite small, being no more than 5 microns in size. Powdered crystals were prepared for UV-Vis absorption. Specifically, the emission spectra of only the MOCha compound **1** can be observed in the visible light spectrum when illuminated with ultraviolet (UV) light. Notably, compound **4** under UV light excitation exhibits weak yellow photoluminescence, with a maximum emission peak at 589 nm (Fig. 4.2E in green) and a photoluminescent quantum yield of only 1% [55]. It is also the only compound in the series that is reactive under UV light, as captured by the power samples image in Fig. 4.2F. Meanwhile, compounds **1**-**3** show negligible interaction under UV excitation. Finally, structural resolution–a crystallographic technique– is used to determine the precise atomic arrangements via the diffraction pattern of the crystal. Fig. 4.2G-J briefly highlight the structurally resolved images of compounds **1**-**4**. While 4.2G and 4.2J clearly indicate stable 2D and 1D inorganic structures, respectively, compounds **2** (Fig. 4.2H) and **3** (Fig. 4.2I) feature buckling in the 2D structure. These results contribute to the ongoing dialogue on the role that ligand functionalization plays in the resulting crystallite morphology and photoluminescent properties of MOChas.

Structural Analysis

The inorganic topologies of the AgS structures are quite striking as the series progresses from 2D to 1D. The position of the functional groups in compounds **2** and **3** perturbs the 2D inorganic in such a way that its topology appears to buckle, capturing the idea of static structures frozen by molecule selection that display a characteristic distortion across the AgS series.

Fig. 4.3 highlights the progression for the inorganic connectivity across the AgS series. Fig. 4.3A shows the 2D sheet of **1**, with edge-sharing tetrahedral surfaces. This feature is characteristic of the typical 2D inorganic connectivity, similar to that of mithrene [56, 57], tethrene and thiorene [57], and a handful of other 2D organofluorine structures [33]. Meanwhile, Fig. 4.3B highlights the slight buckling in the 2D sheet of **2**, characterized by the large open rings in the structure highlighted in light blue. Rather than purely edge-sharing tetrahedra, **2** also features extremely distorted AgS trigonal planes, as indicated by the red triangles over the polyhedral illustration. Ghost bonds, shown in dashed and dotted lines, complete the connections that would form the tetrahedra in a typical 2D inorganic structure, with dashed lines indicating forward projections and dotted lines being the backward projections (Fig. 4.3B, top right panel). It is revealed that Ag atoms which move out of the typical 2D position (boxed inset with red arrows of Fig. 4.3B) cause the large open rings (Fig. 4.3B, top left panel) and therefore a slight buckling in the 2D structure. However, this inorganic connectivity is still somewhat mainly 2D.

Large buckling of the 2D inorganic structure in **3** is visualized in Fig. 4.3C in the bottom left boxed inset panel. The connectivity here is quite unusual–from polyhedral illustration along the *a*-lattice vector, four edge-connected tetrahedra (Fig. 4.3C, top right panel) have silver-sulfur bonds alternating top and bottom of every other pair of sulfur atoms, connected to either bent or flattened trigonal pyramidal inorganic geometries. Above this edge-sharing tetrahedral motif, distorted, flattened trigonal pyramids (red triangles) are connected to the forward-projecting sulfur atoms of the motif, while bent geometries (blue lines) are connected to the bottom forward-projecting sulfur atoms. The reverse is true for backward-projecting sulfur atoms: the tetrahedral motif is connected to bent geometries for *top* sulfur atoms and flattened trigonal pyramidal geometries for *bottom* sulfurs. This pattern then tiles the periodic space. It is theorized that the large buckling in the 2D structure from the giant inorganic rings (Fig. 4.3C, top left panel) is due to the central hydrogen intermolecular forces between the neighboring amines (Fig. 4.3C, middle inset boxed in blue), which form a helical tube in the center of the unit cell. This weak hydrogen-interacting core is parallel to the 2D plane and aligned with the low-density part of the inorganic, therefore giving rise to the presence of intermolecular forces in this region. Finally, Fig. 4.3D shows the 1D rods of **4**, indicated by tubes of connected trigonal planes. The inorganic tube is distorted from a square into a rhombus when viewed along the a-lattice vector (Fig. 4.3D, bottom panel). The trigonal planes create a sheared inorganic core, or one that is not necessarily "upright" but slanted along the vertical tube (Fig. 4.3D, top panels).

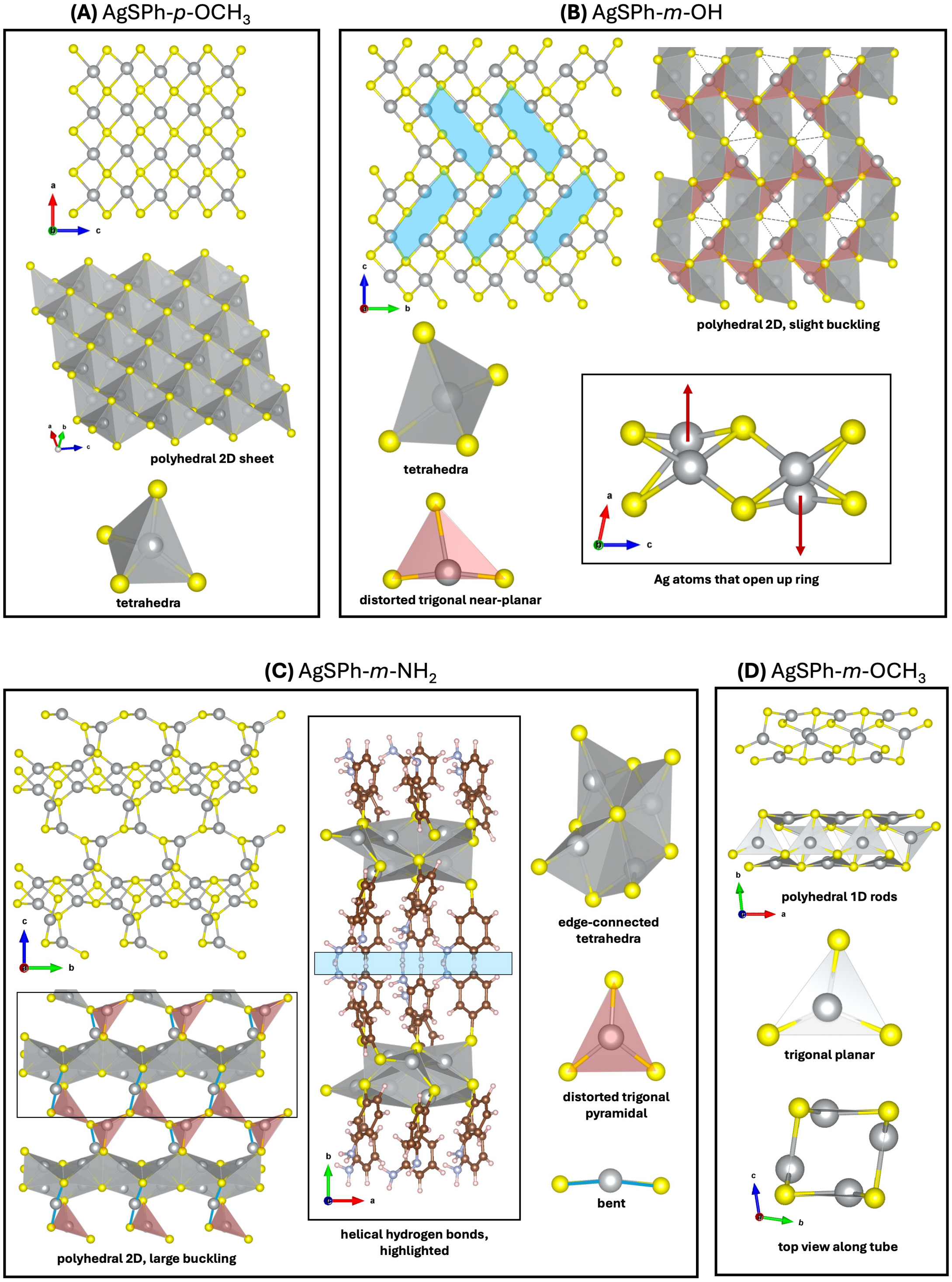
(A) AgSPh-p-OCH3
a
c
polyhedral 2D sheet
tetrahedra
(B) AgSPh-m-OH
c
b
polyhedral 2D, slight buckling
tetrahedra
a
c
Ag atoms that open up ring
distorted trigonal near-planar
(C) AgSPh-m-NH2
c
b
polyhedral 2D, large buckling
b
a
helical hydrogen bonds, highlighted
edge-connected tetrahedra
distorted trigonal pyramidal
bent
(D) AgSPh-m-OCH3
b
a
polyhedral 1D rods
trigonal planar
c
b
top view along tube

Figure 4.3: Structural arrangement of the various AgSPh-X inorganic AgS topologies. **(A)** 2D sheet of AgSPh-*p*-OCH_3, with edge-sharing tetrahedral surfaces. **(B)** Slight buckling in the 2D sheet of AgSPh-*m*-OH, characterized by the large open rings in the structure highlighted in light blue. Red triangles over the polyhedral illustration demonstrate the pattern of trigonal, near-planar geometry. Grey dashed and dotted ghost bonds show the typical 2D inorganic connectivity. **(C)** Large buckling of the 2D inorganic structure in AgSPh-*m*-NH_2. Highlighted red triangles and blue lines in the polyhedral illustration show the presence of trigonal pyramidal and bent geometries, respectively. **(D)** 1D rods of AgSPh-*m*-OCH_3, signaled by tubes of connected trigonal planes.

Energetics with 2D and 1D Models

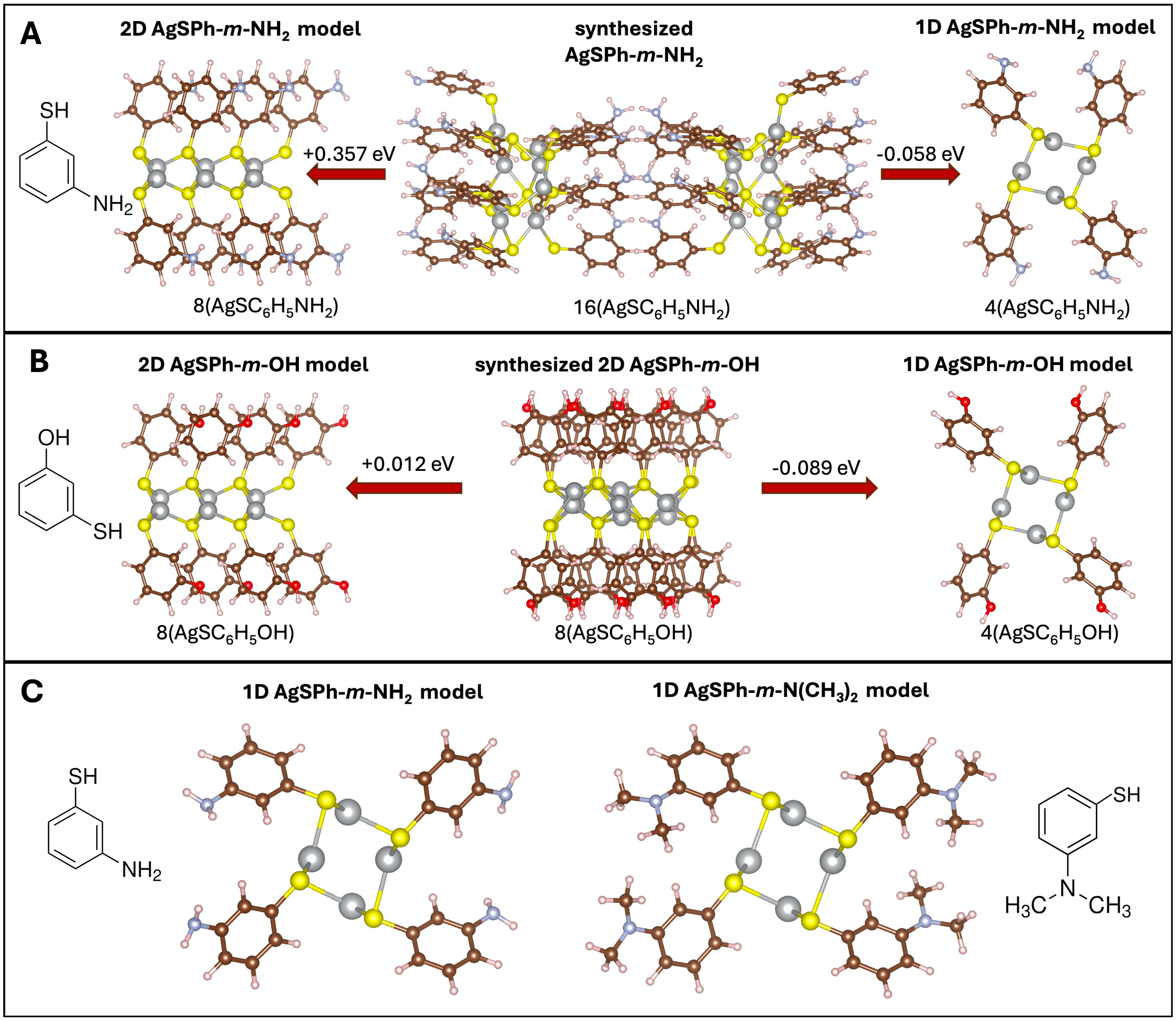
A
2D AgSPh-*m*-NH_2 model
synthesized AgSPh-*m*-NH_2
1D AgSPh-*m*-NH_2 model
SH
NH_2
+0.357 eV
-0.058 eV
8($AgSC_6H_5NH_2$)
16($AgSC_6H_5NH_2$)
4($AgSC_6H_5NH_2$)
B
2D AgSPh-*m*-OH model
synthesized 2D AgSPh-*m*-OH
1D AgSPh-*m*-OH model
OH
SH
+0.012 eV
-0.089 eV
8($AgSC_6H_5OH$)
8($AgSC_6H_5OH$)
4($AgSC_6H_5OH$)
C
1D AgSPh-*m*-NH_2 model
1D AgSPh-*m*-$N(CH_3)_2$ model
SH
NH_2
SH
H_3C
N
CH_3

Figure 4.4: DFT self-consistent field calculations on relaxed geometries, highlighting the energy difference per formula unit between the transitional AgSPh-m-NH_2 and its 2D and 1D homologues of the same ligand **(A)**. The same is done for AgSPh-m-OH **(B)**. **(C)** Hypothetical MOCha models of the 1D AgS structure paired with 3-aminothiophenol (left) and 3-(dimethylamino)thiophenol (right), the latter of which has a crystallographically-unresolved structure.

DFT modeling of hypothetical MOChas supports the inorganic progression from 2D to 1D quite well. To evaluate the energetic differences between experimentally-realized and hypothetical MOChas, we take the ligands containing m-NH_2 and m-OH functional groups and attach them to inorganic 1D and 2D silver sulfide templates from the experimentally-realized compounds **1** (2D) and **4** (1D) as shown in Fig. 2.1B. An SCF calculation is performed on the relaxed geometries of hypothetical 2D and 1D AgSPh-m-OH and AgSPh-m-NH_2, as well as the original experimentally-realized **2** and **3**. Comparing the energetics per formula unit in Fig. 4.4A, we see that the hypothetical 2D silver AgSPh-m-NH_2 MOCha is 0.357 eV higher in energy per formula unit than the experimental compound **3**, whereas the hypothetical 1D silver AgSPh-m-NH_2 MOCha is 0.058 eV lower in energy per formula unit compared to the experimental **3**. Similarly, the hypothetical 2D AgSPh-m-OH MOCha is 0.012 eV higher in energy per formula unit than the experimental compound **2**, whereas the hypothetical 1D AgSPh-m-OH is 0.089 eV lower per formula unit than the experimental **2** (Fig. 4.4B). The modeling reveals that both compounds **3** and **2** are energetic intermediates between the hypothetical 2D and 1D models, and further suggests that the 2D topology and the 1D topology are the stable beginning and end of a series of possible inorganic distortions.

In particular, DFT predicts that the 1D topology is the most energetically-favorable configuration for the Ph-m-NH_2 and Ph-m-OH ligands. For compound **3**, specifically, we hypothesize that neighboring amine hydrogens, which form weak intermolecular forces (Fig. 4.3C, middle inset of compound **3** boxed in light blue), drive the kinetic formation of compound **3**, locking the inorganic structure in its energetically-unfavorable buckling configuration. By disrupting these weak hydrogen interactions, we can force **3** into its lower-energy 1D homologue. This hypothesis led our experimental colleagues to synthesize silver 3-(dimethylamino)thiophenolate (AgSPh-m-$N(CH_3)_2$)–with a ligand quite similar to that of compound **3** but with methyl groups in place of the amine hydrogens (Fig. 4.4C, right panel). We propose that the methyl groups are able to disrupt the weak hydrogen bonding and collapse the inorganic structure from that of compound **3** to a 1D topology. While the actual structure for this new AgSPh-m-$N(CH_3)_2$ compound is yet to be resolved, its crystallite morphology reveals a 1D-like habit analogous to that of Fig. 4.2D, showcasing the power of DFT predictions in driving experimental work. This evidence validates our hypothesis that the forces between interacting amine hydrogens were at least partially responsible for the large buckling in the inorganic structure. Furthermore, this confirms that disrupting the hydrogen interactions of compound **3** by replacing the amine hydrogens with methyl groups indeed leads to a crystallite morphology that is likely 1D, supporting the DFT prediction that the 1D topology is the most energetically-favorable.

Electronic Structure

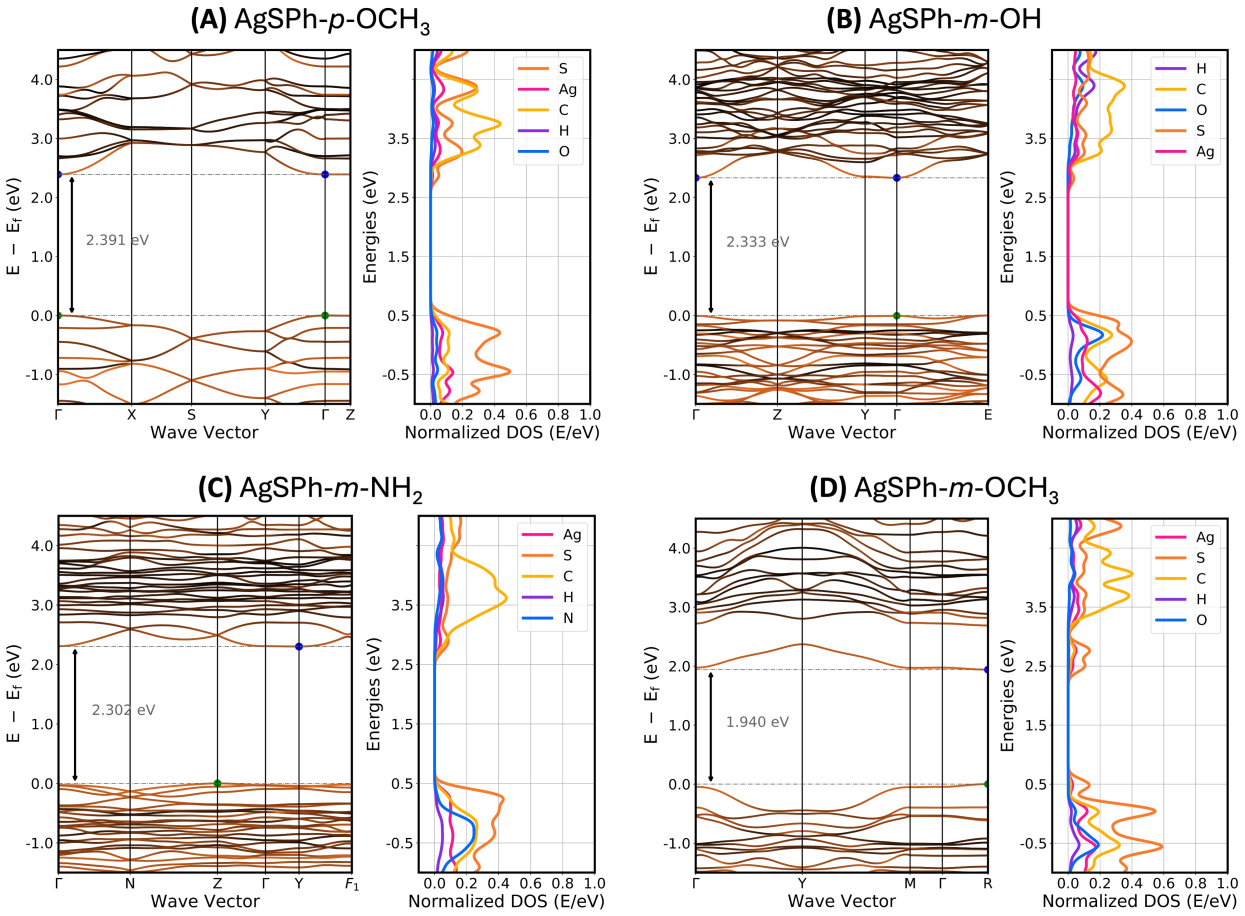

Figure 4.5: **(A-D)** Electronic structure calculations for the AgSPh-X series. Left inset is the band diagram, in which orange bands indicate inorganic interaction and black bands indicate organic interaction, with interpolated colors representing mixed interaction. Blue and green points indicate the wave vector where the conduction band minimum and valence band maximum occur, respectively. Right inset is the normalized density of states, separated by atomic species. Note that figures with a larger number of bands correspond to MOChas with a larger number of atoms.

1 has a direct band gap transition at the Γ point, with a band gap of 2.391 eV (Fig. 4.5A, left). Inorganic interaction (orange) dominates at both the valence and conduction band edges. This can be verified by the density of states diagram (Fig. 4.5A, right), in particular where the largest volume of orbitals belongs to the sulfur atoms. Given the Brillouin zone k-path (Fig. C.1A), the $\Gamma-Z$ path travels along the plane perpendicular to the 2D sheet, and electronic bands are rather flat along this path. Contrastly, the $\Gamma-Y$ and $\Gamma-X$ paths, corresponding to paths in-plane with the 2D sheet, are much more dispersive, indicating more mobile electrons along these regions. The inorganic-only band structure (Fig. C.2A) features an effectively direct band gap transition at the Γ point with a width of 2.408 eV, slightly smaller than that of the original **1**, indicating that the presence of p-OCH_3 in the ligands reduces the band gap width compared to the inorganic-only band structure.

2 has a band gap of 2.333 eV, with an effectively direct band gap transition at the Γ point (Fig. 4.5B, left). Inorganic interaction dominates at both the valence and conduction band edges (orange). In the density of states diagram (Fig. 4.5B, right), again sulfur atom orbitals dominate in the valence band, with smaller Ag and S densities present in the conduction band. The Brillouin zone *k*-path (Fig. C.1B) shows $\Gamma - \mathrm{Y}$ as perpendicular to the plane of the slightly-buckled 2D sheet, and similar to **1**, the inorganic bands at the band gap are rather flat along this path. Along the Γ-Z *k*-path, which is in-plane with the 2D sheet, the conduction band is far more dispersive than the valence band, indicating more electron mobility in the CBM along this region. The inorganic-only band structure (Fig. C.2B) features a direct band gap transition at the Γ point with a width of 2.112 eV, suggesting that the addition of *m*-OH functional groups in the ligands increases the band gap from the inorganic-only structure.

3 has a band gap of 2.302 eV, with an indirect band gap transition from the Z wave vector in the valence band to the Y wave vector in the conduction band (Fig. 4.5C, left). Inorganic interaction appears to dominate at the valence band edges (orange), and slight inorganic-organic mixing occurs at the conduction band edge (dark orange). This can be verified by the density of states diagram (Fig. 4.5C, right), in which the presence of S orbitals dominates in the valence band, and Ag, S, C orbitals appear in the conduction band. The $\Gamma - \mathrm{N}$ path in the Brillouin zone (Fig. C.1C), lies perpendicular to the buckling 2D inorganic plane and is quite dispersive in the conduction band. Similarly, the Γ-Z path features a dispersive conduction band edge, though the valence band edge is relatively flat. The inorganic-only band structure (Fig. C.2C) features a direct band gap transition effectively at the Γ point with a width of 1.830 eV. This width is smaller than that of its parent MOCha's band gap of 2.302 eV, and suggests that *m*-NH_2 functional groups in the ligands increase the band gap width and force an indirect band gap, possibly requiring electron-phonon coupling analysis to unveil these properties in **3**.

4 has a direct band gap transition at the R wave vector, with a band gap of 1.940 eV (Fig. 4.5D, left). Inorganic interaction dominates at both the conduction and valence band edges (orange). This can be verified by the density of states diagram (Fig. 4.5D, right), in which the presence of S orbitals dominates in both the valence and conduction bands. The $\Gamma - \mathrm{M}$ *k*-path (Fig. C.1D) is perpendicular to the inorganic tube and features relatively flat bands, whereas the $\Gamma - \mathrm{Y}$ *k*-path (Fig. C.1D) corresponds to the direction in the original lattice that is along the inorganic tube. Along $\Gamma - \mathrm{Y}$ the bands are very dispersive, indicating higher electron mobility along the tube. The inorganic-only band structure (Fig. C.2D) features an effectively direct band gap transition with a width of 2.045 eV, indicating that *m*-OCH_3 functional groups in the ligands shrink the band gap of the inorganic structure.

We note that there is a trend in decreasing electronic band gap width from the 2D to 1D structures (Fig. 4.5), in which the contribution at the band gap edges remains largely inorganic. The only exception is compound **3**, which features some carbon orbitals in the conduction band edge (Fig. 4.5C, right). The decreasing trend in band gap supports the progression in inorganic dimensionality from 2D to 1D. From the band structure and density of states diagrams, contribution at the band edges from the functional group atoms (e.g. the atoms of OCH_3, OH, and NH_2) is negligible, suggesting that for the silver benzenethiolate series, the functional group may drive the structural formation of these MOChas, but does not explicitly participate in the resulting electronic structure properties.

Interestingly enough, this trend of decreasing band gap from 2D to 1D topologies holds for all inorganic-only band structures except for **3**, whose inorganic-only band gap width is the smallest of the four (Fig. C.2C). Coincidentally, **3** is the only MOCha in this series that features non-inorganic electronic interactions at the conduction band, hinting that this may be responsible for the disruption in inorganic band gap trends. The inorganic-only band gap widths of **1** and **4** (Fig. C.2A,D) are also wider than those of the full thiolated MOCha structure (Fig. 4.5A,D), indicating that the presence of the methoxy series functional group may contribute to the shrinking band gap. Conversely, the inorganic-only band gap widths of **2** and **3** are augmented with the addition of ligands containing m-OH and m-NH$_2$ functional groups, despite having the same *meta* position as m-OCH$_3$. This suggests that the selection of the functional group, rather than the specific position, may contribute to changes in the electronic band gap between the inorganic-only and the full band structure.

Additionally, the direct band gap transition of the 1D compound **4** may elucidate the electronic origins of fluorescence in this MOCha. The same should therefore be expected of the 1D compound **1**—with the same methoxy functional group species and direct band gap transition—but the lack of fluorescence in the latter structure hints at the importance of functionalization on the *meta* and *para* positions around the phenyl ring, resulting in different inorganic topologies and therefore, different structural, electronic, and luminescent properties.

Partial Charge Densities

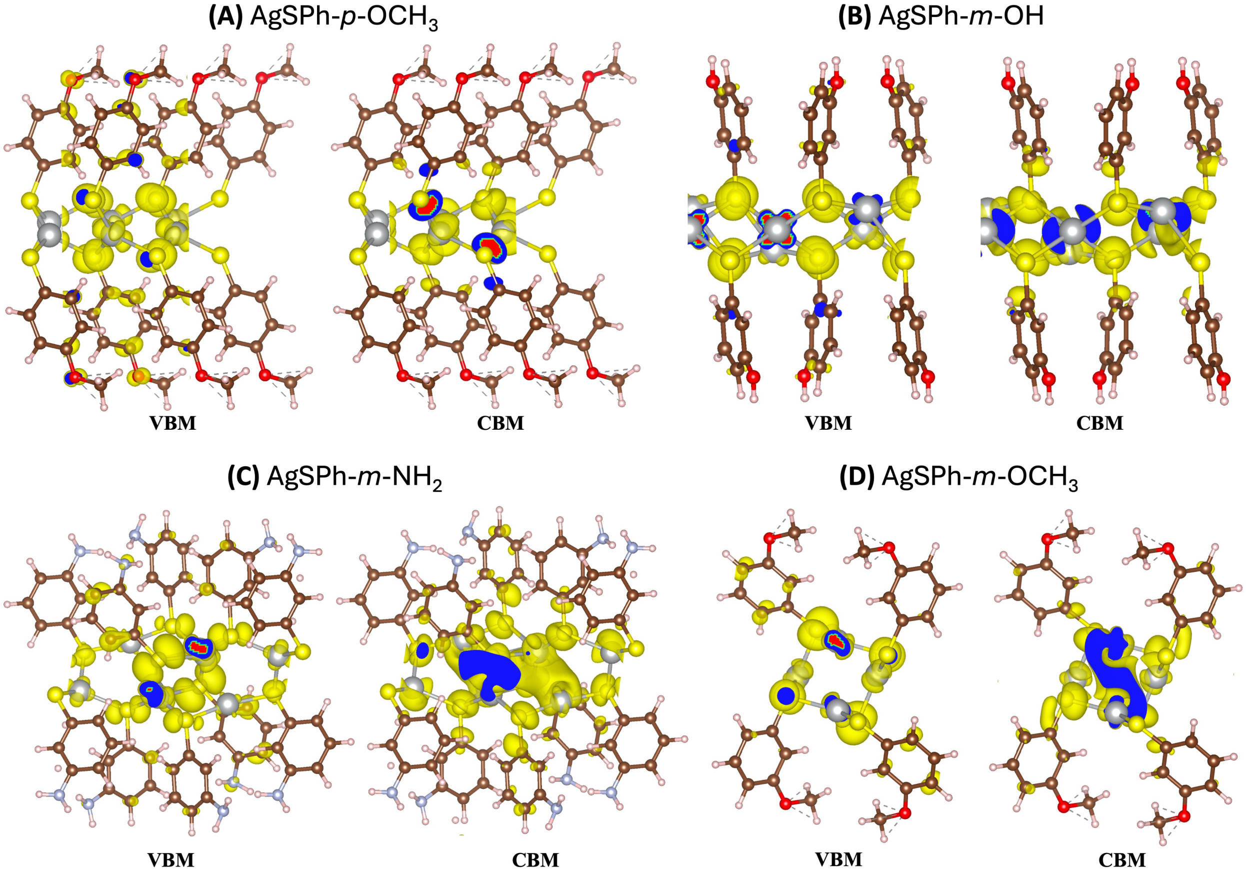

Figure 4.6: Partial charge densities at the valence band maximum (VBM) and conduction band minimum (CBM). **(A)** AgSPh-*p*-OCH_3. **(B)** AgSPh-*m*-OH. **(C)** AgSPh-*m*-NH_2– note that the other half of the motif for the unit cell is omitted for clarity. **(D)** AgSPh-*m*-OCH_3.

In the VBM of compound **1** (Fig. 4.6A), Ag(d) and S(p) orbitals are highly localized. p-orbitals from the phenyl ring appear on the C^1, C^2, C^4, and C^6 atoms, as well as on the oxygen atom in the methoxy functional group. In the CBM, Ag(d) and S(p) orbitals are still localized, though lobes of the Ag(d) orbitals are polarized towards the neighboring S atom, and S(p) orbitals polarize to the neighboring Ag atom. Additionally, weak interactions between the C^1 atom's C(p) orbital in the phenyl ring and the neighboring S(p) orbital are observed, and contribution from the remaining ligand atoms is negligible.

Compound **2** contains mostly tetrahedral geometries, but slight buckling in the 2D structure results in some distorted trigonal planar connectivity (Fig. 4.3B, top right panel). Again, in the VBM of compound **2** (Fig. 4.6)B), Ag(d) and S(p) orbitals are highly localized. Contribution from the phenyl rings is present in the C^4 and C^6 atoms, while negligible O(p) orbitals appear minimally. Strikingly, in the conduction band, electron delocalization appears in Ag(d) orbital lobes, specifically between the distorted trigonal planar Ag atom and its nearest neighbor tetrahedral Ag atom (shown in blue circles in Fig. C.3), suggesting that distortion in the 2D inorganic sheets closes the distance between neighboring Ag atoms and leads to electronic orbital overlap. Polarized S(p) lobes point towards the delocalized Ag(d) electronic overlap, and there are weak interactions between the C^1 atom's C(p) orbital in the phenyl ring and the neighboring polarized S(p) orbital.

In **3** (Fig. 4.3C), the inorganic structure contains a mix of tetrahedral (grey), trigonal planar (red triangles), and bent geometry (blue lines). In the VBM, there is minimal Ag(d) orbital contribution of the trigonal planar and bent AgS geometries compared to the Ag(d) tetrahedral orbitals. S(p) orbital lobes are weakly polarized towards the tetrahedral Ag(d) orbitals, but otherwise the S(p) orbitals are localized and nonpolar. In ligands where the S(p) orbitals are nonpolar, slight electron delocalization occurs between the C(p) orbitals of the C^1 and C^6 atoms, and there are minimal $C^{3,4}$(p) and N(p) contributions. For ligands whose S(p) orbitals are polarized, only the $C^{4,6}$(p) orbitals participate minimally in the VBM. In the CBM, d-orbitals of trigonal planar Ag atoms form crescent shapes, indicating electron hybridization. d-orbitals of Ag atoms that are in the bent or tetrahedral geometry are delocalized and overlap one another. In particular, electronic overlap occurs between the two Ag atoms that are at a distance of 2.94 Å from one another (that is, within 3.45 Å, or 2 × the van der Waals radius of silver), whereas the Ag(d) orbitals of the other Ag atoms that are not within the 3.45 Å range interact weakly with the Ag(d) electronic overlap. Neighboring inner lobes of S(p) orbitals interact weakly with the Ag(d) orbital delocalization, and weak interactions between this S(p) orbital and neighboring C^1(p) orbitals are also present. Some ligands also contain minimal C(p) orbital contributions on the C^2, C^4, C^5, and C^6 atoms (Fig. 4.6C).

Within **4**, the 1D rods of the inorganic structure feature only trigonal planar AgS connectivity (Fig. 4.3D). In the VBM, all inorganic orbitals are localized, and small C(p) orbitals appear on the C^2, C^4, and C^6 atoms. In the CBM, electronic overlap occurs between the two Ag atoms at a distance of 3.3 Å (within 3.45 Å), whereas the Ag(d) orbitals of the other two Ag atoms that are not within this van der Waals distance interact weakly with the Ag(d) electronic overlap. Inner S(p) orbital lobes are polarized towards the Ag(d) orbital delocalization, and weak interactions between the S(p) orbitals and neighboring C(p) orbital of the C^1 on the phenyl ring are also present. We see that the electron orbitals at the conduction band edge are very localized in the 2D **1** compared to the orbital mixing that occurs at both the metal and ligand sites of the 1D **4**. Furthermore, the sturdy and consistent trigonal planar topology of the 1D rods in **4**, direct band gap transition, and orbital delocalization participating at the band edges may also explain the luminescence in **4** and lack thereof in the other structures.

Complementary to the band diagrams for the silver benzenethiolate series, DFT partial charge density calculations revealed that there is increasingly more electron delocalization of electron orbitals at the conduction band across the silver benzenethiolate series as the 2D topology begins to buckle into 1D rods. Again, electron orbitals at the band edges are also largely inorganic. In agreement with the band structure and density of states diagrams, contribution at the band edges from the functional group atoms is negligible, with the exception of **3** which features C(p) orbitals present in both the valence and conduction bands (Fig. 4.6). As mentioned previously, this indicates that while the functional group does not explicitly participate in the resulting electronic structure properties, it plays a significant role in the structural formation of silver benzenethiolate MOChas.

4.4 Conclusions

In this work, we demonstrate that the ligand functional group X plays a critical role in determining the topology of silver benzenethiolate MOChas. To confirm this, we create hypothetical 2D and 1D AgSPh-X MOChas for the m-NH$_2$ and m-OH functional groups using inorganic AgS templates that were derived from experimentally-realized MOChas. Performing DFT self-consistent field calculations on the relaxed geometries reveals that compounds **2** and **3** are energetic intermediates between the 2D and 1D prototypes. In particular, we focus on **3**, and suggest that weak hydrogen intermolecular forces between neighboring amine groups lock **3** in an energetically-unfavorable configuration. We hypothesize that disrupting these weak hydrogen interactions can collapse **3** into a 1D MOCha. This analysis prompted experimentalists to synthesize a similar compound to **3**, with m-N(CH$_3$)$_2$ as the functional group that disrupts weak hydrogen interactions. While the structure is still unresolved, its habit is 1D, validating the DFT prediction that the 1D topology is the most energetically-favorable. Furthermore, DFT-based electronic structure calculations of compounds **1**-**4** reveal trends in the electronic band gap, orbital delocalization at the conduction band, and luminescence across the AgS series that support the progression from 2D to 1D inorganic dimensionality.

Chapter 5

AI'll be back– machine-learning accelerated materials design

In this work, we have understood the tunable optoelectronic properties of the robust, self-assembling, and hybrid materials that are MOChas. From Ch. 3, we have seen that a change as simple as the position of a hydroxyl group in glucose and galactose–ligands that are stereoisomers of each other– result in MOChas with vastly different structural resolutions and optical properties. While both structures were fluorescent 1D topologies, silver(I) thioglucose dihydrate yielded blue photoluminescence while silver(I) thiogalactose dihydrate yielded green photoluminescence. In Ch. 4, we observed that simply varying the position and type of a functional group on a phenyl ring ligand can influence the resulting silver-sulfur inorganic topology, creating a range of possible distortions in the silver benzenethiolate MOCha series.

By manipulating the coordination modes, ligand choice, and selection of coinage metals, we can tune the resulting luminescent, electronic, and structural characteristics for a wide variety of MOChas. This tunable relationship between MOCha structural arrangements and targeted properties opens up a vast yet challenging search space for novel MOCha structures. In addition to the selection of functional groups, functional group positions, and ligands, procurement of physical materials and successful metal-ligand combination experiments take particular consideration and time. Considering all of these parameters together then creates a design space for MOChas that is very difficult to explore experimentally. Computational searches of materials can often be more efficient and cost-effective than experiments, as they allow for rapid exploration of a wide range of systems, frequently yielding intriguing results and occasionally uncovering potential new materials. For example, computational structure searching can augment experimental studies when the data is incomplete or sparse. In the case of MOChas, while over tens of new structures have been resolved since the beginning of the MOChas project, vast metal-ligand combinations remain in uncharted territory, but computational tools can help automate this process.

The task of computationally discovering MOChas is still quite challenging. One must also consider ligand packing patterns, possible inorganic distortions, and unit cell stacking patterns that periodically tile the crystal space. Additionally, materials generation demands the construction of novel and chemically-valid geometries that incorporate various complexities of MOCha properties, including metallophilic interactions, hydrogen bonding, and van der Waals forces. Current attempts to construct hypothetical MOChas involve substitution of inorganic species and ligands with the aid of a coordinate skeleton followed by DFT relaxation of these hypothetical structures. We saw this in action in Section 4.3, where hypothetical 1D and 2D homologues for 3-aminothiophenolate and 3-hydroxythiophenolate were constructed, relaxed, and then energetically evaluated with DFT. In this chapter, we discuss how to enable high-throughput design methods for MOChas such as generative models. Ground state configurations of these generated novel structures could then be obtained via DFT relaxations. However, while DFT can predict properties of materials with good accuracy and is a powerful choice for even hypothetical materials, DFT relaxation times scale poorly for large systems and therefore impede the discovery of novel MOChas structures. To address this computational bottleneck, we discuss the use of machine-learned interatomic potentials (MLIPs) to reduce DFT workloads. The aim of this ML-accelerated workflow is to enable rapid prototyping of novel MOChas. We can propose these structures as new synthesis directions to experimental collaborators, thereby promoting the development of the MOChas field. This work can then be extended to other functional materials with the same prospective applications.

5.1 Structure Generation for Novel Materials

While generative methods are an important avenue for molecular generation, these methods face exceptional obstacles for materials. Complex materials such as MOChas, Metal-Organic Frameworks (MOFs), and Transition Metal Complexes (TMCs) are much larger systems than small molecules, with many more elements, and training data for ML materials design can be limited, as is the case with MOChas. Additionally, because crystalline materials are expressed through periodic transformations, simple 3D molecular generation methods cannot be used as they do not consider periodic transformation invariance [58]. However, in recent years, significant efforts have been made in tackling this problem. Materials generation methods for MOChas can be derived from existing tools that can automate the discovery of novel MOCha structures and functional materials.

Ab-Initio Random Structure Search (AIRSS) is one such computational tool that can generate candidate inorganic structures for MOChas through the use of potential energy surfaces. AIRSS has been used to explore and predict stable crystal structures from first principles, without the need for any prior experimental data or assumptions about the atomic arrangement [59]. It has been instrumental in predicting novel superconductors, 2D materials, and high-pressure phases, and enabled screening of thousands of candidates to identify promising structures. AIRSS generates multiple atomic arrangements randomly by sampling the potential energy surface. The generated structures can follow certain constraints, such as imposed symmetry, stoichiometries, or number of units, to guide the search. Each structure is relaxed using DFT to reach a local minimum in the potential energy surface. Low-energy structures are kept for further analysis, while high-energy ones are discarded as they are not considered energetically stable. Then, a list of stable and metastable crystal structures is produced, which can guide experimental synthesis by predicting the most likely phases to appear under certain conditions.

Another promising method for materials generation of MOChas is the Crystal Diffusion Variational Autoencoder (CDVAE) [60], which generates materials in the form of 3D graph representations. CDVAE functions by learning from the data distribution of stable materials, in which the VAE generates lattice parameters, randomly initializes atom coordinates, and iteratively refines atom coordinates via score matching models [58]. CDVAE also explicitly encodes operations across periodic boundaries, with strengths in generating valid, diverse, and realistic materials, as well as materials that optimize a targeted property. Similar to CDVAE is Symat [61], whose advantage over CDVAE is that it achieves invariance to translations because it applies score matching to pairwise distances (versus CDVAE, which only applies score matching to atom coordinates) [58]. SyMat is therefore invariant to all symmetry transformations on materials. When utilized on the datasets Perov5, a set of 18,928 perovskite materials that share the same structure but have different compositions [62], and MP-20, a set of 45,231 materials that differ in both structure and composition [63], both CDVAE and SyMat outperform other generation methods in at least 5 of the 7 validity metrics (i.e. composition validity, structure validity, etc.). Because of these advantages, CDVAE and SyMat are situated to be promising candidates for proposing novel MOCha structures.

Another future avenue of materials generation could be through learnable shape grammars. Guo *et al.* [64] propose a data-efficient property predictor that can generate molecules from grammar production rules, which outperforms a wide spectrum of baselines, including supervised and pre-trained graph neural networks. This grammar representation of the molecules induces an explicit geometry of the space of molecular graphs, in which graph neural diffusion on the geometry can be used to effectively predict property values of molecules on small training datasets. While this approach is also promising, the previous problems concerning materials generation still apply– encoding transformations across periodic boundary conditions, chemically-valid ligand geometries, and packing patterns. Currently, we are fostering early collaborations with fellow shape grammar specialists to translate MOCha geometries into shape grammar representations.

Ideal models, whether through AIRSS, SyMat, or shape grammars, will be able to generate novel inorganic structures and eventually, novel ligand packing patterns at the appropriate chalcogen sites.

5.2 Fine-tuned ML-interatomic potentials

The majority of this thesis is indeed based on DFT, which we have demonstrated to be a fantastic choice for modeling the electronic structure of experimentally-realized materials, relaxing geometries, and even predicting hypothetical materials. However, anyone working closely with DFT methods for large structures can agree that despite its accuracy, DFT relaxation can be computationally intensive and slow down progress for materials characterization, analysis, and generation. For example, the hydrated glucose MOCha system discussed in Ch. 3 is exactly 205 atoms in size. Coupled with this large system size, DFT-D3 long-range dispersion corrections and hours-long queue wait times for computing resources resulted in the glucose MOCha taking weeks to relax for even the simple ionic loop precision of 0.01 eV/Å! As such, the discovery of novel MOCha structures is hindered by the computational bottlenecks associated with DFT relaxations. One can imagine that this bottleneck would scale poorly for the vast number of hypothetical MOChas produced with generative models, all of which would need to be relaxed to obtain their ground-state optimized geometries. Machine-learned interatomic potentials (MLIPs) can fill this gap in DFT by optimizing the geometry of structures while reducing the computational demands required by the highly-accurate but computationally-intensive modeling methods of DFT.

A possible solution lies in testing EquiformerV2, an equivariant transformer model that iterates on its predecessor, Equiformer, which has demonstrated the efficacy of applying transformers to 3D atomistic systems. EquiformerV2 incorporates higher degrees of equivariant representations [65]. By leveraging higher degrees, the architectural improvements offer speed-accuracy trade-offs, better data efficiency, and a 2× reduction in DFT calculations needed for computing adsorption energies compared to its state-of-the-art competitors. Here, we siphon directly from the work of Open Direct Air Capture 2023 (ODAC23) [66], which consists of more than 38M DFT calculations on more than 8,400 MOFs containing adsorbed CO_2 and/or H_2O. In particular, MOFs, due to their porous nature, have been widely studied as modular adsorbents for capturing pollutants, such as CO_2, from ambient air (known as direct air capture, or DAC). EquiformerV2 is trained on the ODAC23 dataset to approximate calculations at the DFT level, and can perform the tasks of geometry optimization, adsorption energy prediction, and force field development.

From the work of ODAC23, we are interested in the geometry optimization task. We aim to fine-tune an EquiformerV2 model trained on ODAC23 such that it can successfully relax MOCha geometries. We can then assess whether this fine-tuned model can perform ML-based structure relaxations comparable to DFT-calculated results. The goal is to significantly reduce the computational wall time required for MOCha relaxations, which would allow for a faster screening of available generated structures. Early developments in this project have confirmed details that can simplify this fine-tuning task: (i) all the atomic species present in MOChas are also present in the ODAC23 dataset, so the trained EquiformerV2 model will not have to learn any new species mapping and (ii) the DFT relaxations in ODAC23 use the same PBE functional [17] and DFT-D3 dispersion corrections [25] as the MOCha calculations in this thesis. Successful implementation would generate reasonable, relaxed MOCha structures (i.e., without "explosive" atomic migrations during relaxation), providing sufficiently presentable results for experimental synthesis, even if perfect packing is not achieved.

5.3 Closing Remarks

Looking forward, we hope to extend this current research to create fast feedback loops between ML-accelerated materials design, experimental synthesis, and DFT-based characterization of materials. Specifically, we aim to create a rapid prototyping workflow for MOChas that can (i) generate valid inorganic topologies, (ii) generate ligands at the appropriate chalcogen sites of generated inorganic topologies, and (iii) relax and screen chemically and periodically valid hypothetical MOChas constructed from methods (i) and (ii) using ML interatomic potentials. The generated chemically-valid structures can then be proposed to experimentalists for synthesis, promoting seamless integration between computational predictions and experimental validation and accelerating the discovery of novel functional materials.

Appendix A

Relevant Terms

A.1 Relevant Terms

- **CBM** - conduction band minimum
- **CHGCAR** - a file that stores the charge density and the PAW one-center occupancies
- **DOS** - density of states
- **ENMIN/ENMAX** - the minimum or maximum plane-wave energy cutoff in eV for the POTCAR it is read from
- **POSCAR** - an input file that contains the lattice geometry and the ionic positions
- **POTCAR** - an input file that contains the pseudopotential for each atomic species as listed in order in the POSCAR
- **SCF** - self-consistent field
- **SEM** - scanning electron micrograph
- **WAVECAR** - an input file for a continuation job, which contains the number of bands, initial energy cut-off, initial basis vectors defining the supercell, initial eigenvalues, initial Fermi-weights, and initial wave functions
- **VBM** - valence band maximum

Appendix B

Appendix for Don't Sugar Coat it..or do...

B.1 Figures

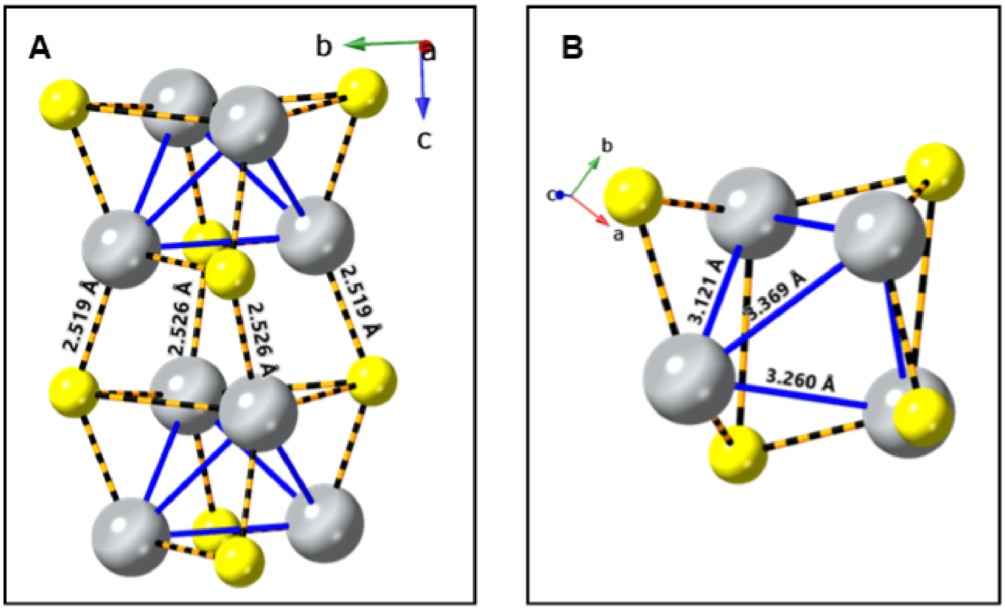
A
b
a
c
2.519 Å
2.526 Å
2.526 Å
2.519 Å
B
b
c
a
3.121 Å
3.369 Å
3.260 Å

Figure B.1: **(A)** The inorganic nanowire of compound **1** consists of repeating Ag_4S_4 units. The Ag_4S_4 units are linked via four Ag-S bonds, forming a 1D chain. **(B)** Each Ag_4S_4 unit features a chiral pyramidal Ag_4 core where each silver atom is coordinated to two or three other silver atoms at different Ag-Ag distances. Color code: Ag, Silver; S, Yellow.

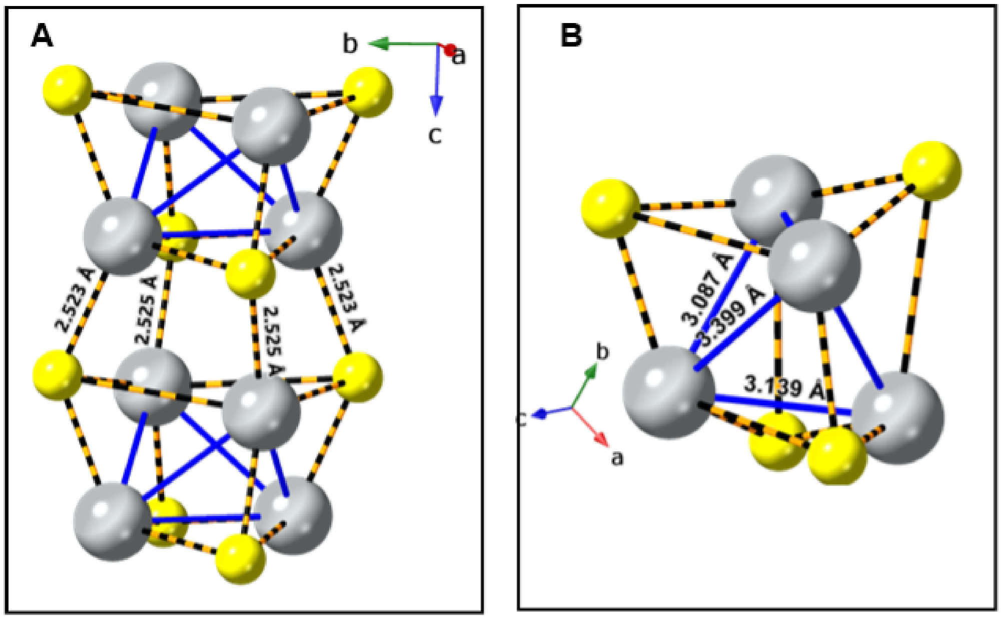
A
b
a
c
2.523 Å
2.525 Å
2.525 Å
2.523 Å
B
3.087 Å
3.399 Å
3.139 Å
b
c
a

Figure B.2: The inorganic AgS core of compound **3** retains a similar 1D Ag-S arrangement as compound **1**, composed of repeating Ag_4S_4 units **(A)** with chiral pyramidal Ag_4 motifs **(B)**. Color code: Ag, Silver; S, Yellow.

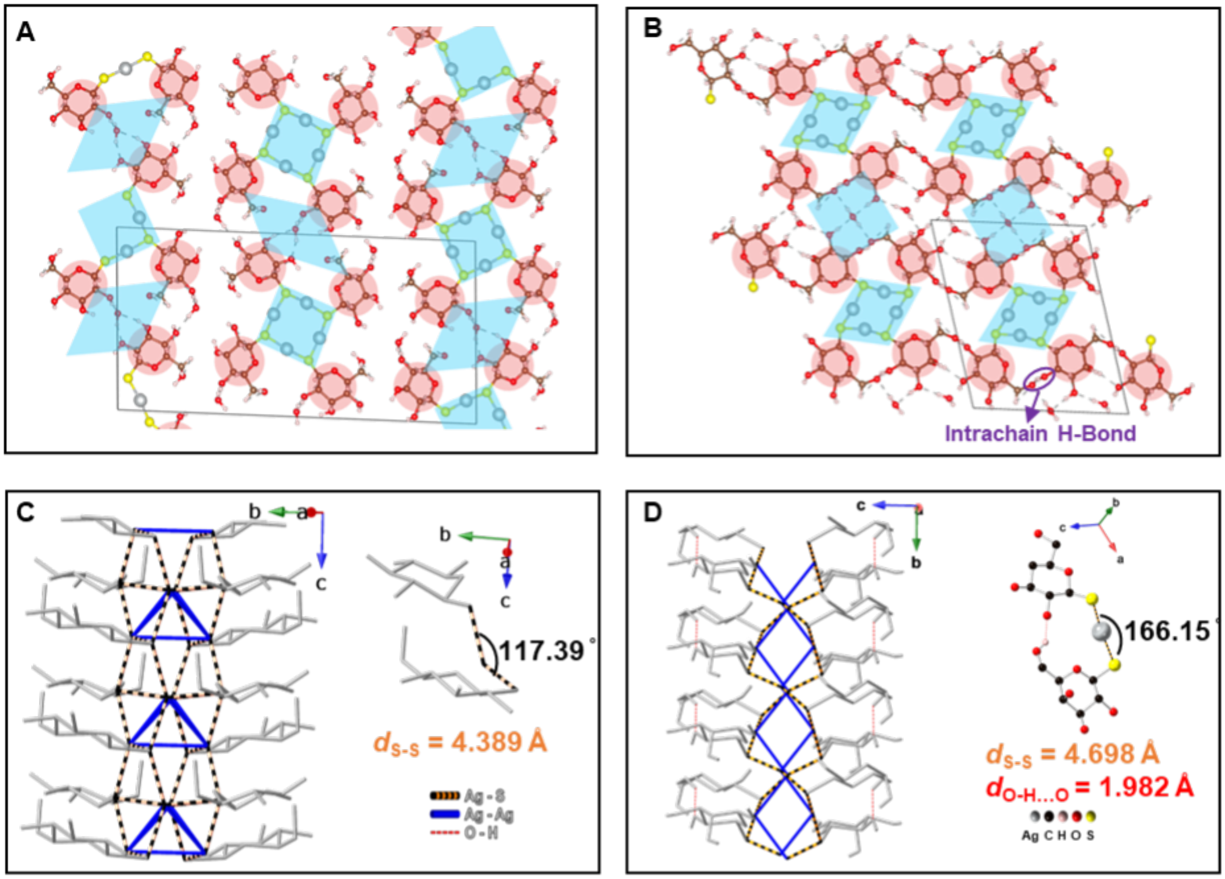
A
B
Intrachain H-Bond
C
b
a
c
117.39°
d_{S-S} = 4.389 Å
Ag-S
Ag-Ag
O-H
D
c
b
a
166.15°
d_{S-S} = 4.698 Å
$d_{O-H...O}$ = 1.982 Å
Ag C H O S

Figure B.3: **(A)** Compound **1** is viewed along the *c* axis and **(B)** Compound **2** is viewed along the *b* axis. Light blue polygons highlight the inorganic topologies and hydrogen bonding interactions of the molecules, whereas light red circles enclose the galactose and glucose ligands. Color code: Ag, silver; S, yellow; O, red; C, brown; H, pink. **(C)** structure of 1D chain unit and S-Ag-S angle in glucose MOCha **1**. **(D)** structure of 1D chain unit and S-Ag-S angle in galactose MOCha **2**. There are H-bonds (OH···O) among ligands and water molecules in both glucose and galactose MOChas. In **2**, there are interchain and intrachain H-bonds, whereas there are only interchain H-bonds in **1**. The O-H···O hydrogen bonds in **2** have a distance of 1.982 Å, indicating directional hydrogen bonds of hydroxyl groups in the sugar ligands. This leads to an increase in the angle of the sulfur-silver-sulfur bond compared to glucose MOCha **1** which lacks interchain hydrogen bonds of the hydroxyl group. As a result, the sulfur-sulfur distance is longer in MOCha **2** (dS-S = 4.698 Å) than in **1** (dS-S = 4.389 Å), decreasing the coordination number of silver-sulfur (CN = 2 in galactose; CN = 3 or 4 in glucose MOCha **1**) and reducing the symmetry of the crystal system compared to the glucose MOCha. In this case, we observed that the secondary structure, driven by the hydrogen bonding network, affects the primary structure of the Ag-S network in a manner similar to biological geometry.

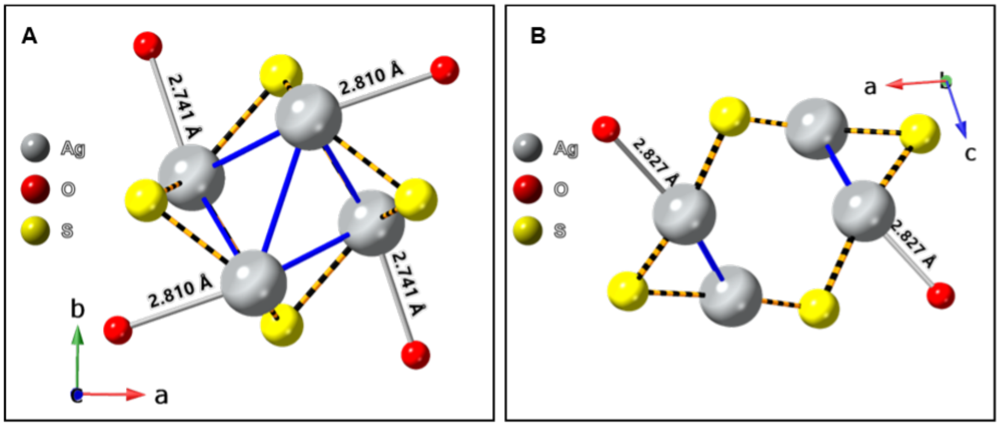

Figure B.4: The Ag-O interaction distances are shown in compounds **1** **(A)** and **2** **(B)**. High luminescence in silver(I) methyl 2-mercaptobenzoate compounds, has been linked to Ag-O interactions, which we recently reported as correlating with relatively high quantum yields. In compounds **1** and **2**, a similar close association is observed between silver and the bridging oxygen atoms of the sugar ligands, with Ag-O bond lengths ranging from 2.741 to 2.827 Å. These distances are notably shorter than the sum of the van der Waals radii (3.24 Å), suggesting the presence of a strong interaction that may contribute to the observed luminescence properties.

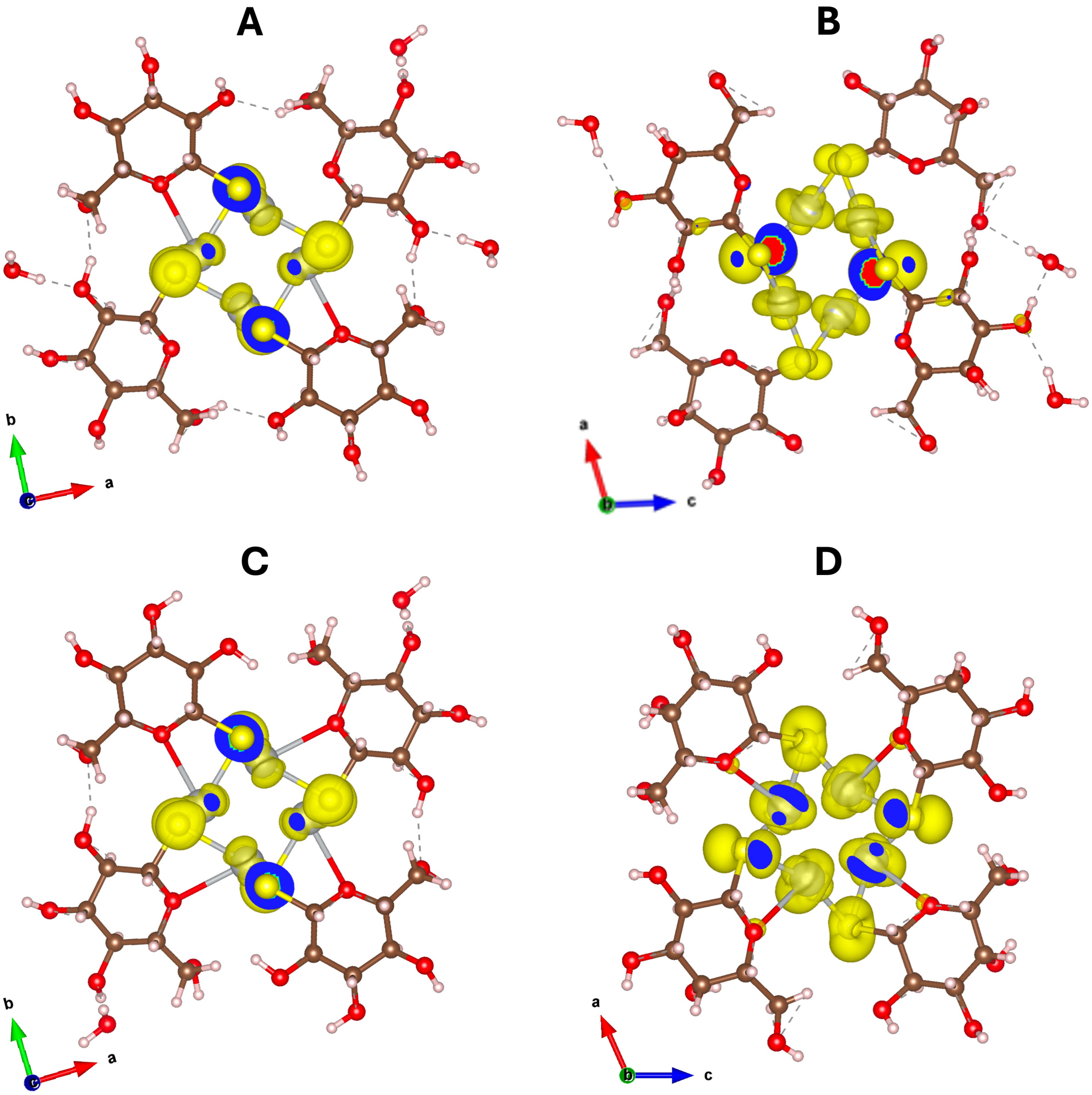
A
b
c
a
B
a
b
c
C
b
c
a
D
a
b
c

Figure B.5: **(A-D)** VBM partial charge densities for each compound **1-4**, respectively, with some other parts of the unit cell and water molecules omitted for clarity.

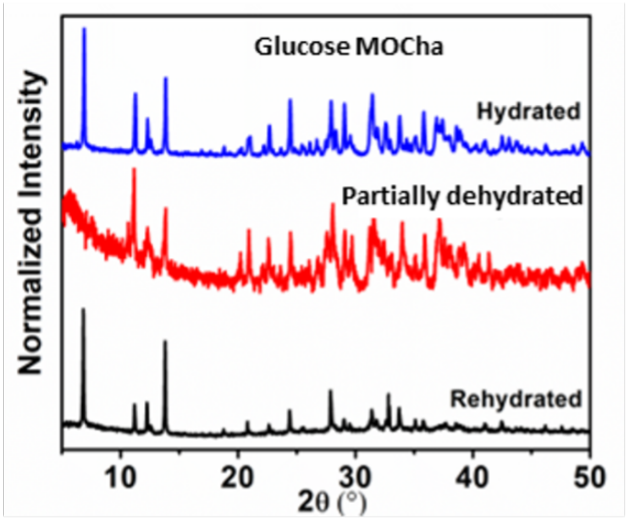

Figure B.6: Comparison of PXRD patterns between as-synthesized hydrated silver thioglucose dihydrate **1**, partially dehydrated silver thioglucose monohydrate **3**, and rehydrated silver thioglucose dihydrate **1**, demonstrating that dehydration and rehydration are reversible.

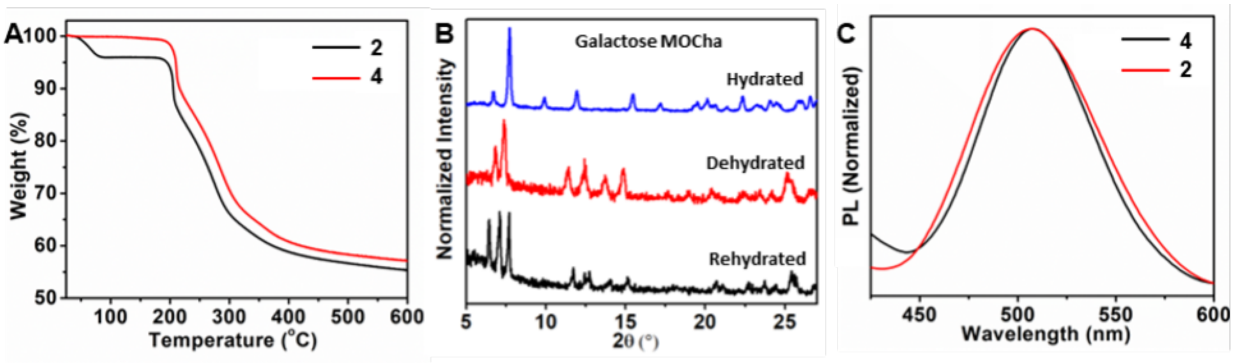

Figure B.7: **(A)** TGA curves of compounds **2** and **4**. **(B)** Comparison of PXRD patterns between as-synthesized hydrated silver thiogalactose dihydrate **2**, fully dehydrated silver thiogalactose **4**, and the rehydrated galactose MOCha. **(C)** Emission spectra comparing the **2** and **4**. The as-synthesized **2** was heated in a vacuum oven at 90 °C for 24 hours to release water, resulting in fully dehydrated samples **4** (Fig. A). PXRD patterns revealed that the **4** exhibits few distinct phases and does not revert to the hydrated state **2** after rehydration, suggesting an irreversible solid-solid phase transformation from galactose MOCha hydrates to dehydrated forms. Fig. **C** shows no significant change in emission between dihydrate **2** and anhydrous **4** under 350 nm excitation.

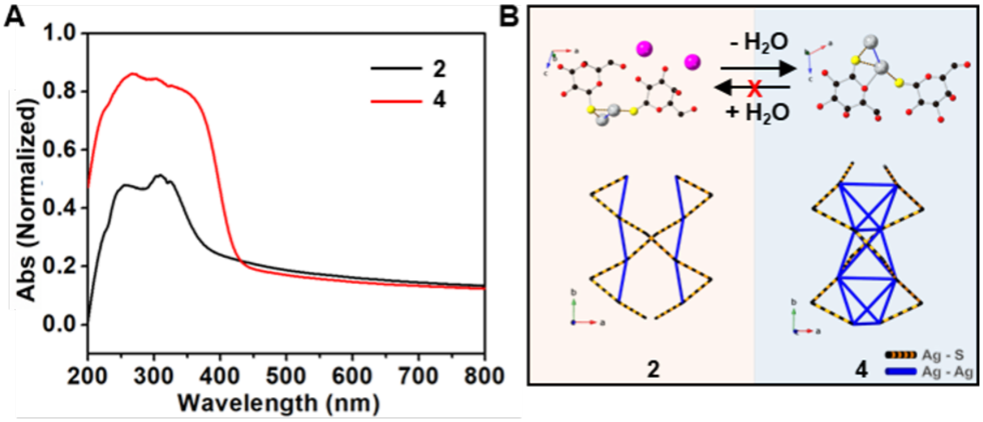

Figure B.8: **(A)** UV-vis spectra comparing compounds **2** and **4**. **(B)** Comparison between **2** (left panel, highlighted in orange) and **4** (right panel, highlighted in blue), focusing on the asymmetry unit (upper panel) and Ag-S network (lower panel). In compound **4**, the Ag-Ag interactions strengthen, forming a coordination number (CN(Ag-Ag)) of 5. This represents a significantly different silver core environment compared to the hydrated form **2** (Fig. **B**), suggesting a change in the electronic structure, indicated by the UV-vis spectrum. Importantly, the change in the Ag-Ag system occurs without altering the inorganic Ag-S arrangement, which remains as double helices. Notably, the asymmetry unit of dehydrated galactose MOCha does not contain water, in line with TGA experiments in Fig. A.

Appendix C

Appendix for Functional Group Drivers and Silver MOCha Passenger Princesses

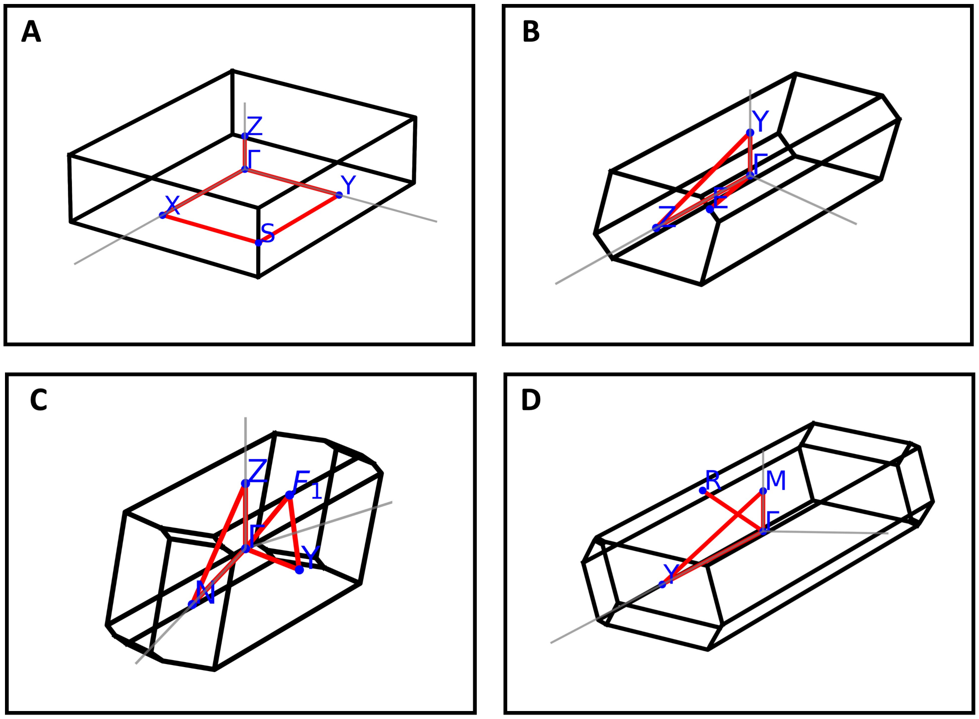
A
Z
Γ
Y
X
S
B
Y
Γ
E
Z
C
Z
F
1
Γ
Y
N
D
R
M
Γ
Y

Figure C.1: Brillouin zones for the selected *k*-paths.

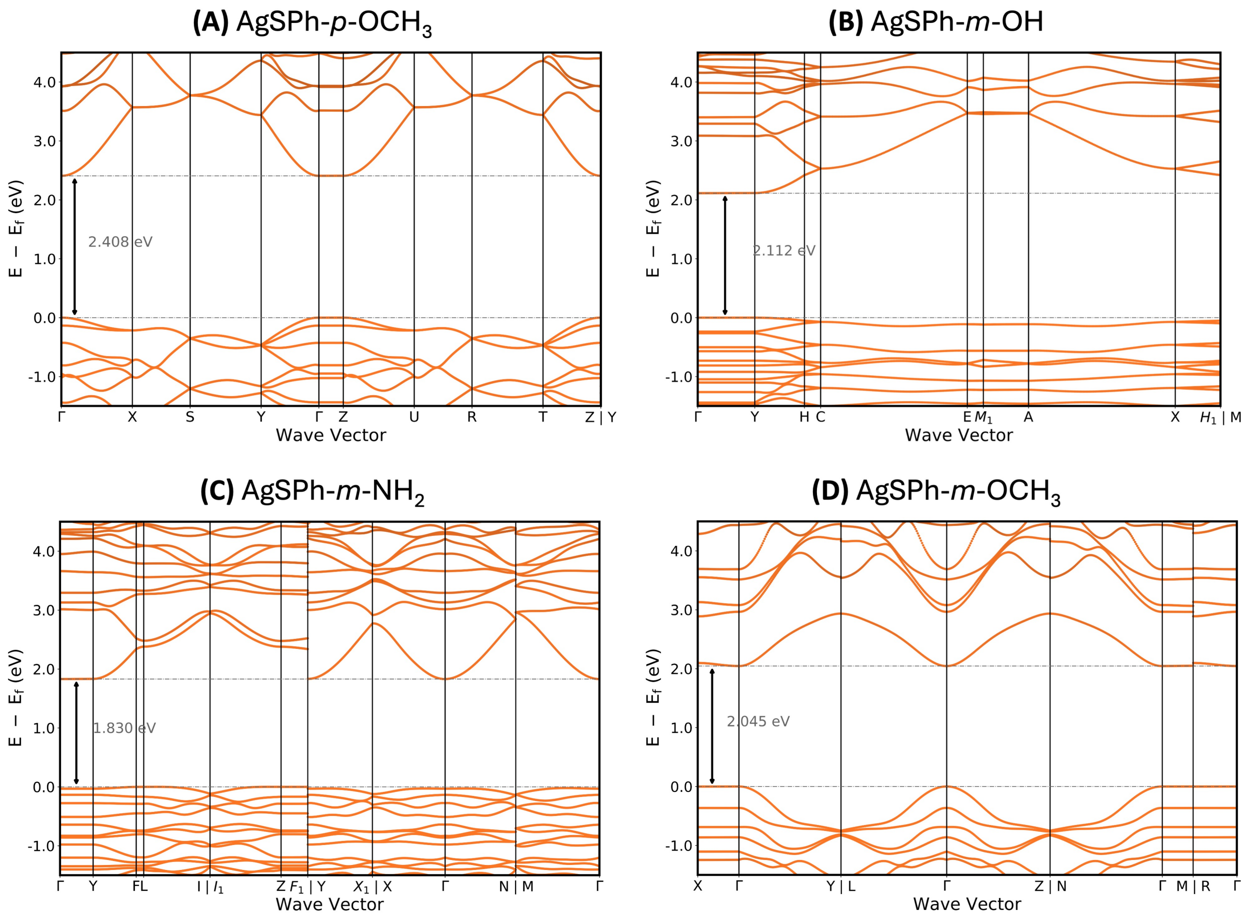

Figure C.2: **(A-D)** Band structure diagrams for the inorganic structure, indicated in orange. All structures effectively have a direct band gap at the Γ point.

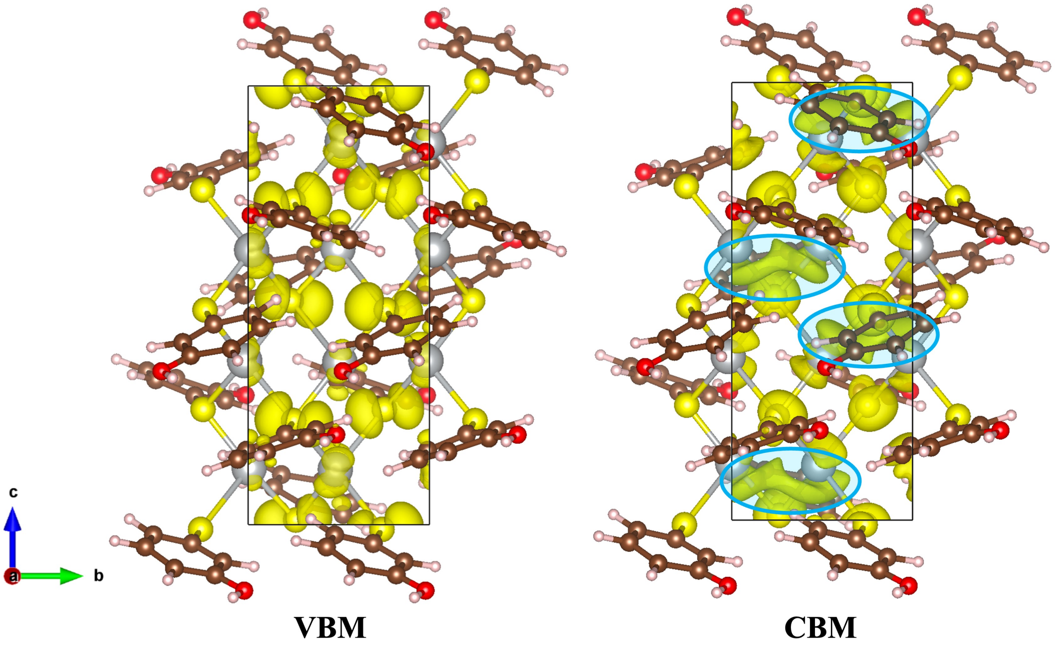

Figure C.3: Partial charge densities at the VBM and CBM for AgSPh-*m*-OH, viewed along the *a*-axis. Electron delocalization of the participating Ag(d) orbitals is encircled in light blue.

References

[1] H. Häkkinen. "The gold–sulfur interface at the nanoscale". In: *Nature Chemistry* 4.6 (2012), pp. 443–455. ISSN: 1755-4349. DOI: 10.1038/nchem.1352. URL: https://doi.org/10.1038/nchem.1352.

[2] I. G. Dance. "The structural chemistry of metal thiolate complexes". In: *Polyhedron* 5.5 (1986), pp. 1037–1104. ISSN: 0277-5387. DOI: https://doi.org/10.1016/S0277-5387(00)84307-7. URL: https://www.sciencedirect.com/science/article/pii/S0277538700843077.

[3] G.-E. Wang, S. Luo, T. Di, Z. Fu, and G. Xu. "Layered Organic Metal Chalcogenides (OMCs): From Bulk to Two-Dimensional Materials". In: *Angewandte Chemie International Edition* 61.27 (2022), e202203151. DOI: https://doi.org/10.1002/anie.202203151. eprint: https://onlinelibrary.wiley.com/doi/pdf/10.1002/anie.202203151. URL: https://onlinelibrary.wiley.com/doi/abs/10.1002/anie.202203151.

[4] O. Veselska and A. Demessence. "d10 coinage metal organic chalcogenolates: From oligomers to coordination polymers". In: *Coordination Chemistry Reviews* 355 (2018). The diversity of coordination chemistry: A special issue in honor of Prof. Pierre Braunstein - Part II, pp. 240–270. ISSN: 0010-8545. DOI: https://doi.org/10.1016/j.ccr.2017.08.014. URL: https://www.sciencedirect.com/science/article/pii/S0010854517303351.

[5] V. W.-W. Yam, V. K.-M. Au, and S. Y.-L. Leung. "Light-Emitting Self-Assembled Materials Based on d8 and d10 Transition Metal Complexes". In: *Chemical Reviews* 115.15 (2015), pp. 7589–7728. ISSN: 0009-2665. DOI: 10.1021/acs.chemrev.5b00074. URL: https://doi.org/10.1021/acs.chemrev.5b00074.

[6] M. Zhang et al. "Processable circularly polarized luminescence material enables flexible stereoscopic 3D imaging". In: *Science Advances* 9.43 (2023), eadi9944. DOI: 10.1126/sciadv.adi9944. eprint: https://www.science.org/doi/pdf/10.1126/sciadv.adi9944. URL: https://www.science.org/doi/abs/10.1126/sciadv.adi9944.

[7] N. Nishizawa and H. Munekata. "Lateral-Type Spin-Photonics Devices: Development and Applications". In: *Micromachines* 12.6 (2021). ISSN: 2072-666X. DOI: 10.3390/mi12060644. URL: https://www.mdpi.com/2072-666X/12/6/644.

[8] B. Ranjbar and P. Gill. "Circular Dichroism Techniques: Biomolecular and Nanostructural Analyses- A Review". In: *Chemical Biology & Drug Design* 74.2 (2009), pp. 101–120. DOI: https://doi.org/10.1111/j.1747-0285.2009.00847.x. eprint: https://onlinelibrary.wiley.com/doi/pdf/10.1111/j.1747-0285.2009.00847.x. URL: https://onlinelibrary.wiley.com/doi/abs/10.1111/j.1747-0285.2009.00847.x.

[9] W. Chen, L. Zheng, M. Wang, Y. Chi, and G. Chen. “Preparation of Protein-like Silver–Cysteine Hybrid Nanowires and Application in Ultrasensitive Immunoassay of Cancer Biomarker”. In: *Analytical Chemistry* 85.20 (2013), pp. 9655–9663. ISSN: 0003-2700. DOI: 10.1021/ac401961f. URL: https://doi.org/10.1021/ac401961f.

[10] H.-B. Yao, M.-R. Gao, and S.-H. Yu. “Small organic molecule templating synthesis of organic–inorganic hybrid materials: their nanostructures and properties”. In: *Nanoscale* 2 (3 2010), pp. 322–334. DOI: 10.1039/B9NR00192A. URL: http://dx.doi.org/10.1039/B9NR00192A.

[11] D. S. Sholl and J. Steckel. “Density functional theory: a practical introduction”. In: John Wiley Sons, Inc, 2009. Chap. 1, pp. 1–32.

[12] W. Kohn and L Sham. “Density functional theory”. In: *Conference Proceedings-Italian Physical Society*. Vol. 49. Editrice Compositori. 1996, pp. 561–572.

[13] P. Hohenberg and W. Kohn. “Inhomogeneous Electron Gas”. In: *Phys. Rev.* 136 (3B 1964), B864–B871. DOI: 10.1103/PhysRev.136.B864. URL: https://link.aps.org/doi/10.1103/PhysRev.136.B864.

[14] J. P. Perdew and K. Schmidt. “Jacob’s ladder of density functional approximations for the exchange-correlation energy”. In: *AIP Conference Proceedings* 577.1 (July 2001), pp. 1–20. ISSN: 0094-243X. DOI: 10.1063/1.1390175. eprint: https://pubs.aip.org/aip/acp/article-pdf/577/1/1/12108089/1_1_online.pdf. URL: https://doi.org/10.1063/1.1390175.

[15] S. F. Sousa, P. A. Fernandes, and M. J. Ramos. “General Performance of Density Functionals”. In: *The Journal of Physical Chemistry A* 111.42 (2007), pp. 10439–10452. ISSN: 1089-5639. DOI: 10.1021/jp0734474. URL: https://doi.org/10.1021/jp0734474.

[16] D. Rappoport, N. R. M. Crawford, F. Furche, and K. Burke. “Approximate Density Functionals: Which Should I Choose?” In: *Encyclopedia of Inorganic Chemistry*. John Wiley Sons, Ltd, 2009. ISBN: 9780470862100. DOI: https://doi.org/10.1002/0470862106.ia615. eprint: https://onlinelibrary.wiley.com/doi/pdf/10.1002/0470862106.ia615. URL: https://onlinelibrary.wiley.com/doi/abs/10.1002/0470862106.ia615.

[17] J. P. Perdew, K. Burke, and M. Ernzerhof. “Generalized Gradient Approximation Made Simple”. In: *Phys. Rev. Lett.* 77 (18 1996), pp. 3865–3868. DOI: 10.1103/PhysRevLett.77.3865. URL: https://link.aps.org/doi/10.1103/PhysRevLett.77.3865.

[18] J. P. Perdew and W. Yue. “Accurate and simple density functional for the electronic exchange energy: Generalized gradient approximation”. In: *Phys. Rev. B* 33 (12 1986), pp. 8800–8802. DOI: 10.1103/PhysRevB.33.8800. URL: https://link.aps.org/doi/10.1103/PhysRevB.33.8800.

[19] S. Kurth, J. P. Perdew, and P. Blaha. “Molecular and solid-state tests of density functional approximations: LSD, GGAs, and meta-GGAs”. In: *International Journal of Quantum Chemistry* 75.4-5 (1999), pp. 889–909. DOI: https://doi.org/10.1002/(SICI)1097-461X(1999)75:4/5<889::AID-QUA54>3.0.CO;2-8. eprint: https://onlinelibrary.wiley.com/doi/pdf/10.1002/%28SICI%291097-461X%281999%2975%3A4/5%3C889%3A%3AAID-QUA54%3E3.0.CO%3B2-8. URL: https:

//onlinelibrary.wiley.com/doi/abs/10.1002/%28SICI%291097-461X%281999%2975%3A4/5%3C889%3A%3AAID-QUA54%3E3.0.CO%3B2-8.

[20] J. P. Perdew. “Accurate Density Functional for the Energy: Real-Space Cutoff of the Gradient Expansion for the Exchange Hole”. In: *Phys. Rev. Lett.* 55 (16 1985), pp. 1665–1668. DOI: 10.1103/PhysRevLett.55.1665. URL: https://link.aps.org/doi/10.1103/PhysRevLett.55.1665.

[21] J. P. Perdew. “Density-functional approximation for the correlation energy of the inhomogeneous electron gas”. In: *Phys. Rev. B* 33 (12 1986), pp. 8822–8824. DOI: 10.1103/PhysRevB.33.8822. URL: https://link.aps.org/doi/10.1103/PhysRevB.33.8822.

[22] J. Heyd, J. E. Peralta, G. E. Scuseria, and R. L. Martin. “Energy band gaps and lattice parameters evaluated with the Heyd-Scuseria-Ernzerhof screened hybrid functional”. In: *The Journal of Chemical Physics* 123.17 (Oct. 2005), p. 174101. ISSN: 0021-9606. DOI: 10.1063/1.2085170. eprint: https://pubs.aip.org/aip/jcp/article-pdf/doi/10.1063/1.2085170/16716890/174101_1_online.pdf. URL: https://doi.org/10.1063/1.2085170.

[23] J. P. Perdew, A. Ruzsinszky, G. I. Csonka, O. A. Vydrov, G. E. Scuseria, L. A. Constantin, X. Zhou, and K. Burke. “Restoring the Density-Gradient Expansion for Exchange in Solids and Surfaces”. In: *Phys. Rev. Lett.* 100 (13 2008), p. 136406. DOI: 10.1103/PhysRevLett.100.136406. URL: https://link.aps.org/doi/10.1103/PhysRevLett.100.136406.

[24] L. A. Curtiss, P. C. Redfern, and K. Raghavachari. “Assessment of Gaussian-3 and density-functional theories on the G3/05 test set of experimental energies”. In: *The Journal of Chemical Physics* 123.12 (Sept. 2005), p. 124107. ISSN: 0021-9606. DOI: 10.1063/1.2039080. eprint: https://pubs.aip.org/aip/jcp/article-pdf/doi/10.1063/1.2039080/15372536/124107_1_online.pdf. URL: https://doi.org/10.1063/1.2039080.

[25] S. Grimme, J. Antony, S. Ehrlich, and H. Krieg. “A consistent and accurate ab initio parametrization of density functional dispersion correction (DFT-D) for the 94 elements H-Pu”. In: *The Journal of Chemical Physics* 132.15 (Apr. 2010), p. 154104. ISSN: 0021-9606. DOI: 10.1063/1.3382344. eprint: https://pubs.aip.org/aip/jcp/article-pdf/doi/10.1063/1.3382344/15684000/154104_1_online.pdf. URL: https://doi.org/10.1063/1.3382344.

[26] G. Kresse and J. Furthmüller. “Efficiency of ab-initio total energy calculations for metals and semiconductors using a plane-wave basis set”. In: *Computational Materials Science* 6.1 (1996), pp. 15–50. ISSN: 0927-0256. DOI: https://doi.org/10.1016/0927-0256(96)00008-0. URL: https://www.sciencedirect.com/science/article/pii/0927025696000080.

[27] W. Setyawan and S. Curtarolo. “High-throughput electronic band structure calculations: Challenges and tools”. In: *Computational Materials Science* 49.2 (2010), pp. 299–312. ISSN: 0927-0256. DOI: https://doi.org/10.1016/j.commatsci.2010.05.010. URL: https://www.sciencedirect.com/science/article/pii/S0927025610002697.

[28] S. P. Ong, W. D. Richards, A. Jain, G. Hautier, M. Kocher, S. Cholia, D. Gunter, V. L. Chevrier, K. A. Persson, and G. Ceder. "Python Materials Genomics (pymatgen): A robust, open-source python library for materials analysis". In: *Computational Materials Science* 68 (2013), pp. 314–319. ISSN: 0927-0256. DOI: https://doi.org/10.1016/j.commatsci.2012.10.028. URL: https://www.sciencedirect.com/science/article/pii/S0927025612006295.

[29] M. D. Hanwell, D. E. Curtis, D. C. Lonie, T. Vandermeersch, E. Zurek, and G. R. Hutchison. "Avogadro: an advanced semantic chemical editor, visualization, and analysis platform". In: *Journal of Cheminformatics* 4.1 (2012), p. 17. ISSN: 1758-2946. DOI: 10.1186/1758-2946-4-17. URL: https://doi.org/10.1186/1758-2946-4-17.

[30] T. A. Halgren. "Merck molecular force field. I. Basis, form, scope, parameterization, and performance of MMFF94". In: *Journal of Computational Chemistry* 17.5-6 (1996), pp. 490–519. DOI: https://doi.org/10.1002/(SICI)1096-987X(199604)17:5/6<490::AID-JCC1>3.0.CO;2-P. eprint: https://onlinelibrary.wiley.com/doi/pdf/10.1002/%28SICI%291096-987X%28199604%2917%3A5/6%3C490%3A%3AAID-JCC1%3E3.0.CO%3B2-P. URL: https://onlinelibrary.wiley.com/doi/abs/10.1002/%28SICI%291096-987X%28199604%2917%3A5/6%3C490%3A%3AAID-JCC1%3E3.0.CO%3B2-P.

[31] A. J. Ladera*, Q. Fan*, D. W. Paley, D. M. Tchoń, A. Rasamsetty, and et. al. "Induced Chirality in Bioinorganic Metal Organic Chalcogenolates Nanowires". In: *preparation for submission* (2025).

[32] T. Sakurada, Y. Cho, W. Paritmongkol, W. S. Lee, R. Wan, A. Su, W. Shcherbakov-Wu, P. Müller, H. J. Kulik, and W. A. Tisdale. "1D Hybrid Semiconductor Silver 2,6-Difluorophenylselenolate". In: *Journal of the American Chemical Society* 145.9 (2023), pp. 5183–5190. ISSN: 0002-7863. DOI: 10.1021/jacs.2c11896. URL: https://doi.org/10.1021/jacs.2c11896.

[33] P. A. Kotei et al. "Engineering Supramolecular Hybrid Architectures with Directional Organofluorine Bonds". In: *Small Science* 4.1 (2024), p. 2300110. DOI: https://doi.org/10.1002/smsc.202300110. eprint: https://onlinelibrary.wiley.com/doi/pdf/10.1002/smsc.202300110. URL: https://onlinelibrary.wiley.com/doi/abs/10.1002/smsc.202300110.

[34] C. Lavenn, N. Guillou, M. Monge, D. Podbevšek, G. Ledoux, A. Fateeva, and A. Demessence. "Shedding light on an ultra-bright photoluminescent lamellar gold thiolate coordination polymer [Au(p-SPhCO2Me)]n". In: *Chem. Commun.* 52 (58 2016), pp. 9063–9066. DOI: 10.1039/C5CC10448C. URL: http://dx.doi.org/10.1039/C5CC10448C.

[35] A. C. Hernandez Oendra, M. A. Aspect, J. L. Jaeggi, J. Baumann, C. R. Lightner, A. B. Pun, and D. J. Norris. "Tunable Synthesis of Metal–Organic Chalcogenide Semiconductor Nanocrystals". In: *Chemistry of Materials* 35.21 (2023), pp. 9390–9398. ISSN: 0897-4756. DOI: 10.1021/acs.chemmater.3c02275. URL: https://doi.org/10.1021/acs.chemmater.3c02275.

[36] Y.-H. Kim et al. "Chiral-induced spin selectivity enables a room-temperature spin light-emitting diode". In: *Science* 371.6534 (2021), pp. 1129–1133. DOI: 10.1126/science.abf5291. eprint: https://www.science.org/doi/pdf/10.1126/science.abf5291. URL: https://www.science.org/doi/abs/10.1126/science.abf5291.

[37] G. Long, R. Sabatini, M. I. Saidaminov, G. Lakhwani, A. Rasmita, X. Liu, E. H. Sargent, and W. Gao. "Chiral-perovskite optoelectronics". In: *Nature Reviews Materials* 5.6 (2020), pp. 423–439. ISSN: 2058-8437. DOI: 10.1038/s41578-020-0181-5. URL: https://doi.org/10.1038/s41578-020-0181-5.

[38] C. Chen, L. Gao, W. Gao, C. Ge, X. Du, Z. Li, Y. Yang, G. Niu, and J. Tang. "Circularly polarized light detection using chiral hybrid perovskite". In: *Nature Communications* 10.1 (2019), p. 1927. ISSN: 2041-1723. DOI: 10.1038/s41467-019-09942-z. URL: https://doi.org/10.1038/s41467-019-09942-z.

[39] A. Pietropaolo, A. Mattoni, G. Pica, M. Fortino, G. Schifino, and G. Grancini. "Rationalizing the design and implementation of chiral hybrid perovskites". In: *Chem* 8.5 (2022), pp. 1231–1253. ISSN: 2451-9294. DOI: 10.1016/j.chempr.2022.01.014. URL: https://doi.org/10.1016/j.chempr.2022.01.014.

[40] J. Ahn, E. Lee, J. Tan, W. Yang, B. Kim, and J. Moon. "A new class of chiral semiconductors: chiral-organic-molecule-incorporating organic–inorganic hybrid perovskites". In: *Mater. Horiz.* 4 (5 2017), pp. 851–856. DOI: 10.1039/C7MH00197E. URL: http://dx.doi.org/10.1039/C7MH00197E.

[41] M. Aleksich et al. "XFEL Microcrystallography of Self-Assembling Silver n-Alkanethiolates". In: *Journal of the American Chemical Society* 145.31 (2023), pp. 17042–17055. ISSN: 0002-7863. DOI: 10.1021/jacs.3c02183. URL: https://doi.org/10.1021/jacs.3c02183.

[42] Z. Fan and A. O. Govorov. "Plasmonic Circular Dichroism of Chiral Metal Nanoparticle Assemblies". In: *Nano Letters* 10.7 (2010), pp. 2580–2587. ISSN: 1530-6984. DOI: 10.1021/nl101231b. URL: https://doi.org/10.1021/nl101231b.

[43] W. Ma, L. Xu, A. F. de Moura, X. Wu, H. Kuang, C. Xu, and N. A. Kotov. "Chiral Inorganic Nanostructures". In: *Chemical Reviews* 117.12 (2017), pp. 8041–8093. ISSN: 0009-2665. DOI: 10.1021/acs.chemrev.6b00755. URL: https://doi.org/10.1021/acs.chemrev.6b00755.

[44] H. Yan et al. "Sterically controlled mechanochemistry under hydrostatic pressure". In: *Nature* 554.7693 (2018), pp. 505–510. ISSN: 1476-4687. DOI: 10.1038/nature25765. URL: https://doi.org/10.1038/nature25765.

[45] H. Yan et al. "Hybrid metal–organic chalcogenide nanowires with electrically conductive inorganic core through diamondoid-directed assembly". In: *Nature Materials* 16.3 (2017), pp. 349–355. ISSN: 1476-4660. DOI: 10.1038/nmat4823. URL: https://doi.org/10.1038/nmat4823.

[46] S. Li, J. Luo, J. Liu, and J. Tang. "Self-Trapped Excitons in All-Inorganic Halide Perovskites: Fundamentals, Status, and Potential Applications". In: *The Journal of Physical Chemistry Letters* 10.8 (2019), pp. 1999–2007. DOI: 10.1021/acs.jpclett.8b03604. URL: https://doi.org/10.1021/acs.jpclett.8b03604.

[47] A. S. Novikov. "Non-Covalent Interactions in Organic, Organometallic, and Inorganic Supramolecular Systems Relevant for Medicine, Materials Science, and Catalysis". In: *Crystals* 12.2 (2022). ISSN: 2073-4352. DOI: 10.3390/cryst12020246. URL: https://www.mdpi.com/2073-4352/12/2/246.

[48] G. C. Roberts, A. Watts, E. B. S. Association, et al. *Encyclopedia of biophysics*. Springer Berlin Heidelberg, 2013.

[49] F. Tian, H. Qu, A. Zimmermann, T. Munk, A. C. Jørgensen, and J. Rantanen. "Factors affecting crystallization of hydrates". In: *Journal of Pharmacy and Pharmacology* 62.11 (2010), pp. 1534–1546. DOI: https://doi.org/10.1111/j.2042-7158.2010.01186.x. eprint: https://onlinelibrary.wiley.com/doi/pdf/10.1111/j.2042-7158.2010.01186.x. URL: https://onlinelibrary.wiley.com/doi/abs/10.1111/j.2042-7158.2010.01186.x.

[50] A. Ladera*, M. Aleksich*, A. Lamonica, T. Smidt, and J. Hohman. "Role of functional group identity at meta position on silver benzenethiolate as a determinant of dimensionality and structural properties in metal-organic chalcogenolates". In: *preparation for submission* (2025).

[51] H. Yang, S. Mandal, Y. H. Lee, J. Y. Park, H. Zhao, C. Yuan, L. Huang, M. Chen, and L. Dou. "Dimensionality Engineering of Lead Organic Chalcogenide Semiconductors". In: *Journal of the American Chemical Society* 145.44 (2023), pp. 23963–23971. ISSN: 0002-7863. DOI: 10.1021/jacs.3c05745. URL: https://doi.org/10.1021/jacs.3c05745.

[52] K. Yao, M. S. Collins, K. M. Nell, E. S. Barnard, N. J. Borys, T. Kuykendall, J. N. Hohman, and P. J. Schuck. "Strongly Quantum-Confined Blue-Emitting Excitons in Chemically Configurable Multiquantum Wells". In: *ACS Nano* 15.3 (2021), pp. 4085–4092. ISSN: 1936-0851. DOI: 10.1021/acsnano.0c08096. URL: https://doi.org/10.1021/acsnano.0c08096.

[53] R. Khamlue et al. "Heterocyclic Modification Leading to Luminescent 0D Metal Organochalcogenide with Stable X-ray Scintillating Properties". In: *Chemistry of Materials* 36.10 (2024), pp. 5238–5249. ISSN: 0897-4756. DOI: 10.1021/acs.chemmater.4c00653. URL: https://doi.org/10.1021/acs.chemmater.4c00653.

[54] C. Kastl, P. Bonfà, and L. Maserati. "Anharmonic Exciton-Phonon Coupling in Metal-Organic Chalcogenides Hybrid Quantum Wells". In: *Advanced Optical Materials* 11.7 (2023), p. 2202213. DOI: https://doi.org/10.1002/adom.202202213. eprint: https://onlinelibrary.wiley.com/doi/pdf/10.1002/adom.202202213. URL: https://onlinelibrary.wiley.com/doi/abs/10.1002/adom.202202213.

[55] M. Aleksich et al. "Ligand-Mediated Quantum Yield Enhancement in 1-D Silver Organothiolate Metal–Organic Chalcogenolates". In: *Advanced Functional Materials* n/a.n/a (), p. 2414914. DOI: https://doi.org/10.1002/adfm.202414914. eprint: https://onlinelibrary.wiley.com/doi/pdf/10.1002/adfm.202414914. URL: https://onlinelibrary.wiley.com/doi/abs/10.1002/adfm.202414914.

[56] E. A. Schriber, D. C. Popple, M. Yeung, M. A. Brady, S. A. Corlett, and J. N. Hohman. “Mithrene Is a Self-Assembling Robustly Blue Luminescent Metal–Organic Chalcogenolate Assembly for 2D Optoelectronic Applications”. In: *ACS Applied Nano Materials* 1.7 (2018), pp. 3498–3508. DOI: 10.1021/acsanm.8b00662. URL: https://doi.org/10.1021/acsanm.8b00662.

[57] E. A. Schriber et al. “Chemical crystallography by serial femtosecond X-ray diffraction”. In: *Nature* 601.7893 (2022), pp. 360–365. ISSN: 1476-4687. DOI: 10.1038/s41586-021-04218-3. URL: https://doi.org/10.1038/s41586-021-04218-3.

[58] X. Zhang et al. *Artificial Intelligence for Science in Quantum, Atomistic, and Continuum Systems*. 2024. arXiv: 2307.08423 `[cs.LG]`. URL: https://arxiv.org/abs/2307.08423.

[59] C. J. Pickard and R. J. Needs. “Ab initio random structure searching”. In: *Journal of Physics: Condensed Matter* 23.5 (2011), p. 053201. DOI: 10.1088/0953-8984/23/5/053201. URL: https://dx.doi.org/10.1088/0953-8984/23/5/053201.

[60] T. Xie, X. Fu, O.-E. Ganea, R. Barzilay, and T. Jaakkola. *Crystal Diffusion Variational Autoencoder for Periodic Material Generation*. 2022. arXiv: 2110.06197 `[cs.LG]`. URL: https://arxiv.org/abs/2110.06197.

[61] Y. Luo, C. Liu, and S. Ji. “Towards Symmetry-Aware Generation of Periodic Materials”. In: *Advances in Neural Information Processing Systems*. Ed. by A. Oh, T. Naumann, A. Globerson, K. Saenko, M. Hardt, and S. Levine. Vol. 36. Curran Associates, Inc., 2023, pp. 53308–53329. URL: https://proceedings.neurips.cc/paper_files/paper/2023/file/a73474c359ed523e6cd3174ed29a4d56-Paper-Conference.pdf.

[62] I. E. Castelli, D. D. Landis, K. S. Thygesen, S. Dahl, I. Chorkendorff, T. F. Jaramillo, and K. W. Jacobsen. “New cubic perovskites for one- and two-photon water splitting using the computational materials repository”. In: *Energy Environ. Sci.* 5 (10 2012), pp. 9034–9043. DOI: 10.1039/C2EE22341D. URL: http://dx.doi.org/10.1039/C2EE22341D.

[63] A. Jain et al. “Commentary: The Materials Project: A materials genome approach to accelerating materials innovation”. In: *APL Materials* 1.1 (July 2013), p. 011002. ISSN: 2166-532X. DOI: 10.1063/1.4812323. eprint: https://pubs.aip.org/aip/apm/article-pdf/doi/10.1063/1.4812323/13163869/011002_1_online.pdf. URL: https://doi.org/10.1063/1.4812323.

[64] M. Guo, V. Thost, S. W. Song, A. Balachandran, P. Das, J. Chen, and W. Matusik. “Hierarchical Grammar-Induced Geometry for Data-Efficient Molecular Property Prediction”. In: *Proceedings of the 40th International Conference on Machine Learning*. Ed. by A. Krause, E. Brunskill, K. Cho, B. Engelhardt, S. Sabato, and J. Scarlett. Vol. 202. Proceedings of Machine Learning Research. PMLR, 2023, pp. 12055–12076. URL: https://proceedings.mlr.press/v202/guo23h.html.

[65] Y.-L. Liao, B. Wood, A. Das, and T. Smidt. *EquiformerV2: Improved Equivariant Transformer for Scaling to Higher-Degree Representations*. 2024. arXiv: 2306.12059 `[cs.LG]`. URL: https://arxiv.org/abs/2306.12059.

[66] A. Sriram, S. Choi, X. Yu, L. M. Brabson, A. Das, Z. Ulissi, M. Uyttendaele, A. J. Medford, and D. S. Sholl. "The Open DAC 2023 Dataset and Challenges for Sorbent Discovery in Direct Air Capture". In: *ACS Central Science* 10.5 (2024), pp. 923–941. ISSN: 2374-7943. DOI: 10.1021/acscentsci.3c01629. URL: https://doi.org/10.1021/acscentsci.3c01629.